Supporting Information for

Interface-Driven Bipolar Photoresponse in a Doping-Engineered n-Type Polymer Enables Single-Layer Retinomorphic Devices

Jiao Suo[1], Yifan Liu[2], Augustine O. Yusuf[3], Kenneth R. Graham[3], Liyan You[1], Inho Song[1, 4,], Jianguo Mei[1,*]*

[1]Department of Chemistry, Purdue University, West Lafayette, IN 47907, USA.
[2]Deptment of Electrical and Computer Engineering, Michigan State University, MI 48824, USA
[3]Department of Chemistry, University of Kentucky, Lexington, KY 40506, USA
[4]Department of Chemical Engineering, Chung-Ang University, Seoul 06974, Republic of Korea

This PDF file includes:

Supplementary Text

Figs. S1 ~ S46

Tables S1-S3

References (#1 to #65)

Downloaded from pubs.acs.org/ancac3/article-supplement/5207499/pdf/nn6c07332_si_001/ by PURDUE UNIV user on 28 October 2026

Supplementary Text

Supplementary Note 1: Functions of bipolar cells in the human retina and inspiration for artificial visual system

In the human retina, there are three separate layers: the distal layer of photoreceptors, the middle layer of interneurons, and the proximal layer of ganglion cells, working together to perform these pre-process functions (Figure S1a)[1]. Photoreceptors convert light information into electrical signals, which are subsequently encoded by bipolar cells into different pathways. These signals are then integrated by ganglion cells to generate the spikes that are transmitted to the brain through the optical nerve[2]. These types of cells form the most direct vertical visual pathway with horizontal cells and amacrine cells provide some complemented lateral interaction[3]. A central computational principle of the retinal circuitry is the antagonistic center–surround organization of receptive fields (RFs), primarily established by bipolar cell signaling[4, 5]. These RFs allow the visual cortical neurons to extract the basic visual features (such as edges, orientations, etc.) through ganglion cells and then performing more advanced processing[6]. Building on this knowledge of human retina and human visual system, one of the most important image recognition models[7], convolutional neural network (CNN), was developed for machine vision system, inspired by this biological computational architecture[8, 9]. Given this shared foundation of visual information processing, both machine vision system and bio-integrated artificial vision system would benefit from the retinomorphic vision sensors with bipolar photoresponse to acquire the structured visual information through the sensor node (for machine vision system) or retina prosthesis (for bio-integrated artificial vision system), shown in Figure S1b. Nevertheless, these two technologies are developed relatively independently, with most reported retinomorphic devices targeting machine vision applications to reduce the system power consumption and latency. Meanwhile, further advances in retina prosthesis for vision restoration remain urgently needed. Previously approved commercial products, Argus II and Alpha-IMS, have been discontinued due to their high cost and limited imaging quality. To achieve next generation biointegrated artificial vision, bio-inspired optoelectronic devices should overcome the key challenges including limited resolution, mechanical and signal mismatch between the optoelectronic devices and the biological visual neuron system[10].

Supplementary Note 2: Comparison of the optoelectronic devices with bipolar photoresponse

Optoelectronic devices with bipolar photoresponse behavior have been reported in different systems. In general, bipolar photoresponse with opponent polarity can be triggered by multidimensional light information (intensity, wavelength, etc.), or the applied electrical signal. The former trigger method is suitable for constructing all-optical computing architecture, where performing logic operation by changing the input light parameters, including light wavelength, intensity or polarization. The later trigger method is suitable for building the reconfigurable vision sensor where the pixel level photoresponsivity can be actively modulated by the applied electrical signals, so that enables them to perform the retinomorphic in-sensor edge enhancement via programming constracting the appropriate kernel. Category of the reported bipolar photoconductive devices according to the trigger mechanism and the corresponding application is summarized in Table S1. We further made a detailed comparison with other reported bipolar photoconductive devices with electrically tunable negative/positive photoresponsivity in Table S2 below. The current primary device configurations are shown in Figure S2, including photogating-based phototransistor, ferroelectric photodiode and spilt-gate modulated photodiode. A radar-chart

Downloaded from pubs.acs.org/ancac3/article-supplement/5207499/pdf/nn6c07332_si_001/ by PURDUE UNIV user on 28 October 2026

comparison of representative devices from these categories is presented in Figure S3, evaluating key performance metrics including the device compactness (represented by 1/T, T: device terminal), fabrication simplicity, array fill factor, operation voltage (represented by 1/|Vmax|), and photoresponsivity range (represented by |Rpositive-Rnegative|). Compared with previously reported device types, the proposed device exhibits relatively lower photoresponsivity, but offers advantages in device compactness, fabrication simplicity, array fill factor and low-operation voltage. To further advance the proposed device toward practical image-sensing applications, several potential approaches could be applied: (1) Like the cornea and crystalline lens of the human eye[11], almost all modern image sensors are coated with an array of micro-lenses (shown in Figure S4a of the Supporting Information) to gather the inside light and focus it on the active pixel, thus improve the effective photosensitive[12, 13]. Similarly, by integrating the microlens and amplifier circuit through system-level design, the photoresponsivity of the image system-based on the proposed device could be improved higher than current reported value. (2) From the device design perspective, Fig. 3A in the manuscript shows that the photocurrent could be modulated by the doping level of the active layer. With decreased doping level, the device exhibits an narrowed bipolar photoresponse range but high photocurrent. The reported photoresponsivity is calculated from the device based on the pristine as-cast n-PBDF thin film. By carefully modulating the doping level of the active layer to balance the bipolar photoresponse range and photocurrent amplitude, the photoresponsive could be improved. (3) The reported photoresponsivity is measured under visible light (532 nm) stimulation, in practical weak-light condition such as night vision, the active near-infrared (NIR) illumination could be employed as a supplementary. The proposed device exhibits its functionality in the NIR wavelength range of 808 nm and 905 nm (Supplementary Fig. S11), which is advantageous for night-time or low-light sensing applications[14-16]. Realizing visual information preprocessing such as edge enhancement through bipolar photoconductive pixels with tailored receptive fields is a bio-inspired strategy that mimics neurobiological architecture. Such biomimetic imaging systems offer a promising solution to the current challenge of high computational demand[17], as demonstrated both in previous bipolar optoelectronic devices and in this work. As we discussed previously, as a biomimic visual perception strategy, such devices are not only promising for the machine vision system but also for retina prosthesis to provide retinomorphic light encoding methods which can be compatible with the peripheral neuronal circuits. This is particularly important since previously approved commercial retinal implants have been discontinued, underscoring the need for new technologies. In this context, our work provides advantages from the following perspectives: 1) Materials perspective. While the conventional photodetectors based on crystalline Group IV or III-V semiconductors[18] give unipolar photoresponse, the bipolar photoconductive optoelectronics are usually based on emerging semiconducting materials, such as two-dimensional semiconductors, halide perovskites, or organic semiconductors. Among them, organic polymers enable biocompatibility, flexibility and light weight, which are desired for implant retina prosthesis as materials fail is one of the main reasons for previous prosthesis failure. Specially, n-PBDF, which the main device based on, has been proved to work well in the biological system in a separate system. 2) Device architecture. The vertical photodiode architecture offers potential of high integration and fill factor compared to lateral structure in phototransistor[19], while the high resolution is a highly problematic obstacle in current retina prosthesis, so photodiode is a desirable architecture in in such application. 3) Simply and cost-effective fabrication benefits both the material and device architecture. The single active layer is solution processible without high temperature growth while its spectrum of the active material could be easily tuned, etc.

Downloaded from pubs.acs.org/ancac3/article-supplement/5207499/pdf/nn6c07332_si_001/ by PURDUE UNIV user on 28 October 2026

Compared to three- or four-terminal gate architecture, the two-terminal device could suffer from the crosstalk and poor selectivity issues for individual programming. However, programmable two-terminal electronic devices are widely used or explored in many fields[7, 20-25], including the image system, where most used modern camera has a two-terminal photodiode as its photodetector and connect transistors in each pixel for selection and amplification. The most recognized solution to mitigate the crosstalk issue of two-terminal electronics is to apply one-transistor-one-resistor architecture (1T1R) one selector-one-memristor (1S1R) structure, which has been used in other two-terminal electronic device systems such as memristor[7, 24] and display[25]. Although additional transistor is needed to achieve precisely pixel control, vertical two-terminal device could still achieve high spatial resolution since the photosensitive pixel array can be connected to the control circuit by several metallization layers so that the photo-sensing layer on the top exposure to the light while the additional control transistor on the separate layer and did not actually limit the sensing resolution (Figure S4a, b)[13]. However, the state-of-art three-terminal phototransistors or four- terminal lateral photodiode have the lateral active channel for light exposure[17, 26-35] (Figure S4c). From this perspective, the vertical two-terminal bipolar photodetector holds promising application in scalability even if precise pixel-level control needs additional transistor/selector. Overall, the lateral arranged sub-pixel structures would decrease spatial resolution, while the vertical two-terminal structure could enhance it. By integrating with advanced thin-film transistor (TFT) technology, improved control of the proposed two-terminal bipolar photodetector can be achieved, similar to that in other two-terminal electronic components (e.g., display pixel[25], memristor[24], etc.). In addition, the photolithography compatible fabrication process would enable the integration. Therefore, we envision that the proposed device could be attributed to the high resolution bipolar photoconductive devices for retinomorphic vision sensors.

Supplementary Note 3: Device with symmetric electrode

It is noticed that symmetric Au and Ag electrode devices have NPC and symmetric ITO electrode has PPC (Figures S14 and S15). NPC is not a common optoelectronic phenomenon compared to the PPC in the conventional photodetectors[36]. In three-terminal devices, NPC can be achieved by the photogating effect[37]. However, some materials are reported to exhibit NPC properties itself[38-40], especially in highly doped materials with a high concentration of carriers[39, 40]. Therefore, this NPC is less observed in organic materials due to its relatively low carriers compared to inorganic materials. The highly conductive polymer n-PBDF with carrier concentration estimated to be 10^{22} cm^{-3} [41, 42] made NPC happen in device with as-cast polymer without further processing. Dedoping the active layer of n-PBDF could make the photoconductive of Au/n-PBDF/Au change from unipolar NPC to unipolar PPC (Figure S16a). So, we hypothesize that the ITO surface captures part of the excess electrons (due to the rough surface or oxygen vacancy), to cause the main PPC in the device. We first tested the ITO/n-PBDF/ITO which shows a PPC. Then, we treated the device with Trimethylhydroquinone (TMHQ) to increase its doping level, and the photoconductance of the device changed to NPC (Figure S16b). Figure S17 shows the X-ray photoelectron spectroscopy (XPS) of the ITO surface. The peak related to the oxygen vacancy[43, 44] is considerable. Therefore, it is reasonable to attribute the main PPC phenomena of ITO-related electrodes to the oxygen vacancy of ITO surface. Regardless of the main photoconductance of NPC or PPC, the symmetric electrode devices show unipolar photoconductance while the asymmetric electrodes show bipolar.

Supplementary Note 4: Metal-Semiconductor-Metal photodiode

The existence and formation of the Schottky junction-based built-in field due to the work function

Downloaded from pubs.acs.org/ancac3/article-supplement/5207499/pdf/nn6c07332_si_001/ by PURDUE UNIV user on 28 October 2026

difference in the metal-semiconductor-metal (MSM) photodiode structure has been well recognized and is a crucial component in optoelectronic devices[45-47]. In MSM structure, asymmetric electrodes naturally lead to asymmetric junctions and an asymmetric photoresponse, which can give rise to bipolar photoresponse when the photodiode operates in the photoconductive mode[46]. However, although such behavior is generally expected, the anticipated impact on the optoelectronic properties may not always manifest in practical devices due to the non-ideal interface formation as reported in [46]. In our results, employing asymmetric electrodes and neutral state P3HT, BBL and PProDOT polymers did not show obvious bipolar photoresponse although they have asymmetric junctions too. A pronounced bipolar photoresponse emerges once they are doped (Figure S13). Therefore, we propose that the highly doped active polymer caused narrow but strong built-in fields at the interfaces, enhancing such effect and enabling a significant bipolar photoresponse in the photoconductive mode. The detection limit of this Schottky junction-based photodiode is analyzed. With the time-dependent photoresponse measurement, the detection limit of the proposed device with pristine n-PBDF as the active layer is estimated to be approximately 120 μW, whose signal-to-noise ratio (SNR) is greater than 3 as shown in Figure S18 To further quantify the detection limit, we analyzed the noise current of the device, which primarily includes shot noise, Johnson noise and flicker noise. The shot noise from the dark current is given by $I_{shotnoise} = \sqrt{2eI_{dark}} \approx 10^{-12}$ (e is the absolute value of electron charge 1.6 x10^{-19} Coulombs and I_{dark} is the dark current). According to the measured total noise current spectrum shown in Figure S19, the frequency dependent flicker noise dominates at low frequency, while the noise current approaches the shot noise limit at higher frequency. Based on the measured total noise current (i_n) and photoresponsivity (R) under the same bias condition (Fig. 2B), the Noise Equivalent Power (NEP) is estimated using $NEP = i_n(1Hz)/R \approx 10^{-6}W/\sqrt{Hz}$. This result indicates a higher minimum detectable optical power and weaker low-light detection capability than the optimized conventional photodiodes. The detectivity of the photodetector could be limited by the three main noise, i.e., shot noise from dark current, Johnson noise and flicker noise[48, 49]. The flicker noise is considered originates from carrier mobility fluctuations from Hooge model or carrier number fluctuations from the McWhorter model, and high carrier scattering could induce the high flicker noise[50, 51]. In addition, the relatively higher dark current of the Schottky junction-based single-layer photodiode typically has lower detectivity than conventional photodiode based on p-n junction[52, 53]. Therefore, the present device is not optimized for its high detectivity and ultra-low light detection capability. The detectivity could be further improved by suppressing the noise current such as reducing the dark current and carrier scattering centers or improving the responsivity such as optimizing the materials doping status. A tradeoff comparison between conventional photodiode and the proposed single layer photodetector is summarized in Table S3. Although the proposed device has lower detectivity, but it has tunable positive and negative photoresponsivity enabling high-efficient neuromorphic vision sensing system.

Supplementary Note 5: Process of implementing convolutional neural network in the proposed device

Downloaded from pubs.acs.org/ancac3/article-supplement/5207499/pdf/nn6c07332_si_001/ by PURDUE UNIV user on 28 October 2026

The flow chart for the implementation of the neural network on the proposed device is shown in Figure S39a, where we use hybrid training and transfer the weight to our device for forward computation. For hardware implemented neural network, ex-situ or hybrid training is generally adopted for convolutional neural network (CNN) training due to the highly complex operation on hardware[7]. In the simpler artificial neural network (ANN), the implementation on the optoelectronic device have certain steps such as the loss calculation performed with software[17]. The proposed array performs convolution by treating light power (P) as the input and responsivity (R) as the weight, where the photocurrent is given by $I_{ph} = P * R$, the multiplication and accumulation required for convolution are naturally achieved through Kirchhoff's law (Figure S39b). In this case, the ability of the device memory for previous configuration is the retention of the device to keep its photoresponsivity under the same applied bias, which can be verified from the time-resolved photocurrent measurement[17]. Figure S39c exhibits that our device could maintain its photoresponse after at least 1200s with electricity disconnected. Another important property for the proposed device to perform the convolution computing is its photoresponsivity can be linearly modulated from -0.87 mA/W to 6.1 mA/W (Figure S39d), which facilitates the ex-situ training and weight transfer. While the results on in-sensor fingerprint minutiae extraction is simulated, we also demonstrated a prototype 3×3 array system to perform the in-sensor classification of two characters based on these properties.

Supplementary Note 6: Simulation of in-sensor fingerprint minutiae discrimination

For the simulation Dataset containing 622 fingerprint images was constructed for the in-sensor discrimination. A in-sensor discrimination neural network was trained to differentiate the images with "Ending" or "Bifurcation" features. We constructed a network containing a convolution layer and a fully connected layer. Without pooling layer, batch normalization or activation function, the network could be simplified to a linear mathematic model as follows:
Input image could be defined as:
$X \in R^{13\times13}$

If we applied 8 convolution kernels with different weight distribution:
$W_i \in R^{3\times3}(i = 1, \dots, 8)$

and corresponding b_i. To avoid the overlap during the convolution, we set the stride as 3 and padding to be 1, the output size would be:
$Y \in R^{8\times5\times5}$

Then the output feature after each kernel could be expressed as:

$$Y_i(p,q) = \sum_{u=0}^{2}\sum_{v=0}^{2} W_i(u,v)X(3p+u-1, 3q+v-1) + b_i \; for \; p,q \; \in \{0,1,2,3,4\}$$

Then all the output would be flattened to input to fully connected layer, the flattened array is defined as $Z_{i,p,q}$

Downloaded from pubs.acs.org/ancac3/article-supplement/5207499/pdf/nn6c07332_si_001/ by PURDUE UNIV user on 28 October 2026

$Z_{i,p,q} = Y_i(p,q)\ for\ i = 1, \ldots, 8\ and\ p,q\ \in \{0,1,2,3,4\}$

Then final output y decides the image to be "Ending" or "Bifurcation" could be expressed as:

$$y = \sum_{u=1}^{8}\sum_{p=0}^{4}\sum_{q=0}^{4} w_{i,p,q} Z_{i,p,q} + c$$

Where $w_{i,p,q}$ represent the weights of the fully connected layer and c is the bias. We can obtain a mathematical model for the complete model as:

$$y = \sum_{u=1}^{8}\sum_{p=0}^{4}\sum_{q=0}^{4}\{\sum_{u=0}^{2}\sum_{v=0}^{2} W_i(u,v) X(3p+u-1, 3q+v-1) + b_i)\} Z_{i,p,q} + c$$

Therefore, the relationship between the final output and each single input of image could help us to decide the real weight for each pixel on sensor to be:

$S_{i,3p+u-1,3q+v-1} = W_i(u,v) Z_{i,p,q}\ for\ p,q\ \in \{0,1,2,3,4\}$

To improve the training efficiency, we assign the same network on computer to simulate the weight $S_{i,3p+u-1,3q+v-1}$ update after each epoch. After we find the best weight after the simulated training, we can locally assign them on our retinomorphic vision sensor implement the in-sensor fingerprint minutiae discrimination. As the classification result could be directly represented by the output photocurrent, we could achieve an analog-based CNN to perform the classification work without any assistance from the computer. With similar ideas, in the hybrid keypoint extraction mode, the retinomorphic vision sensor combining the sensing unit and the first convolution layer. Then the output would be input to computer for further processing, and more information containing the keypoint for minutiae could be provided. The hybrid keypoint extraction mode was trained with the same dataset for the in-sensor minutiae. The whole process is also illustrated in Figure S41.

Supplementary Note 7: Analysis of power consumption of the proposed device and corresponding visual system

By utilizing the bipolar photoconductive optoelectronic devices as the image sensor to perform in-sensor convolutional computation, a more efficient visual perception system could be built by filtering out the redundant data and accelerating the post-processing (Figure S46). Considering on M×N sensor array, a conventional visual perception architecture employs a conventional image sensor that generates M×N data for capturing the information from each single pixel. These unstructured raw data are sequentially transferred to the memory unit for storage, and then transferred to the processing unit for image recognition, etc. In contrast, in the visual perception architecture based on image sensor with in-sensor processing capability, enabled by the bias modulated bipolar photoconductive, the designed convolutional kernel could be implemented on the sensor itself, thereby realizing in-sensor processing. In this scheme, the data can be read out line by line without requiring the data from each single pixel, substantially reducing the volume of data collected at the sensor node. The reduced data volume could further lower both energy

Downloaded from pubs.acs.org/ancac3/article-supplement/5207499/pdf/nn6c07332_si_001/ by PURDUE UNIV user on 28 October 2026

consumption and memory consumption during data transfer and storage. Moreover, the structured data after convoluted would then facilitate the downstream image recognition, leading to improved computational efficiency compared with the unstructured raw data[54]. For example, fewer epochs are required to achieve the same recognition accuracy, as demonstrated by the experiment results in this work. From both data-reduction and computational-efficiency perspectives, the bipolar photoconductive image sensor could help reduce the overall power consumption at the system-level. For the device proposed in this work, as the device operates without the previous programming process, the device could operate in the voltage range within 0.2V. As an active sensing electronic, scaling the voltage is an effective way to decrease the energy power consumption of image system, since the total power consumption could be calculated as $P = P_{dynamic} + P_{static} = \alpha CV^2 f + IV$ (where α is the switching factor, C is the total capacitance load, V is the voltage, f is the operation frequency)[55, 56]. Dynamic power consumption is highly dependent on circuit activity, and the low operation voltage of the device could effectively decrease dynamic power consumption $P_{dynamic} = \alpha CV^2 f$. As a reference, a typical CMOS image sensor (PYTHON300/500/1300) has a voltage and current of the pixel power rail with 3.3 V and 5 mA[57]. At system level, total energy consumption includes multiple components, such as sensing, data storage, data transferring, processing and interfacing with execution motors. The device proposed in this work could principally improve the visual perception efficiency by shifting part of the processing load to the sensing node similar to the human visual system, however, the practical power consumption and efficiency also rely on the co-design of the sensing, memory and processing units.

Downloaded from pubs.acs.org/ancac3/article-supplement/5207499/pdf/nn6c07332_si_001/ by PURDUE UNIV user on 28 October 2026

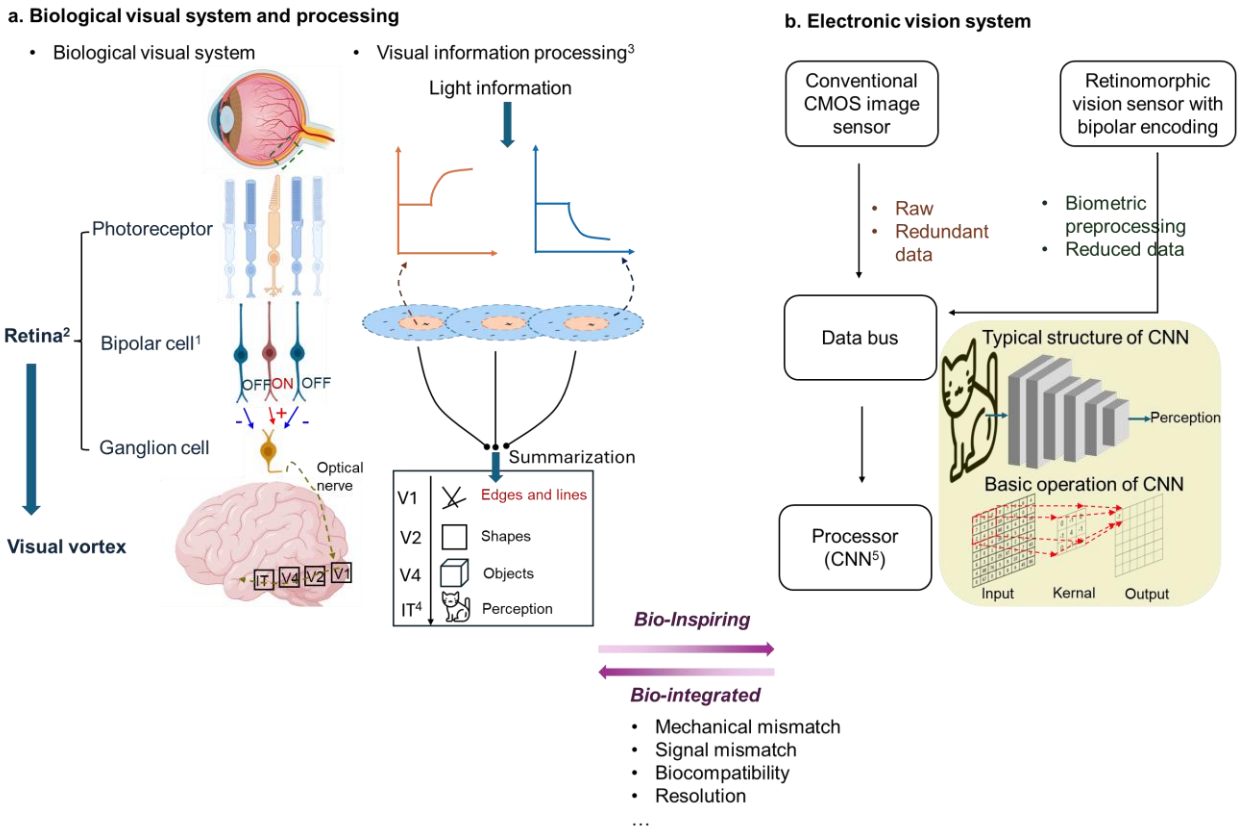

Figure S1. Illustration of the biological visual system and processing pathway (**a**), and electronic vision system and processing pathway (**b**). [1]: As important interneuron type, there are different types of bipolar cells, including chromatic preference, polarity and kinetics. Here we discussed is the polarity bipolar cells.[2]: Here only illustrate the main vertical visual pathway. There are horizontal cells between photoreceptor and the bipolar cells, and amacrine cells between bipolar cells and ganglion cells to provide lateral modulation.[3]: Visual perception involves complex spatial and temporal signal processing, here only illustrate one basic spatial related processing.[4]: IT: Inferotemporal Cortex.[5]: CNN: Convolutional Neural Network.

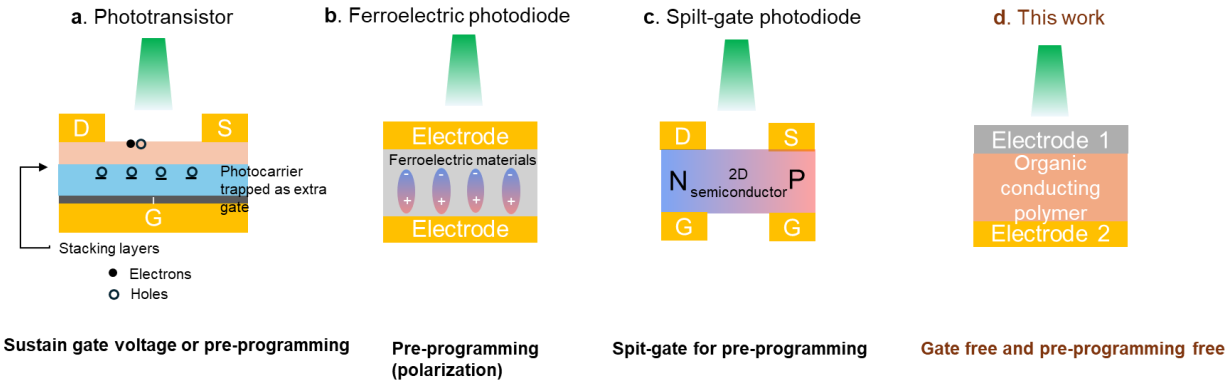

Figure S2. Typical device configuration of electric field modulated bipolar photoconductive device for reconfigurable vision sensor. **a**, Phototransistor based on photogating effect. **b**, Ferroelectric photodiode. **c**, Spilt gate modulated photodiode. **d**, This work.

Downloaded from pubs.acs.org/ancac3/article-supplement/5207499/pdf/nn6c07332_si_001/ by PURDUE UNIV user on 28 October 2026

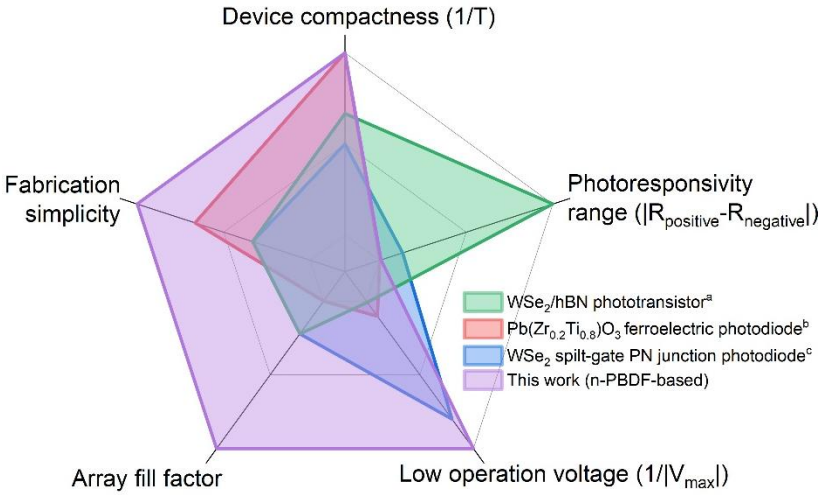

Figure S3. Radar chart to compare the key performance merits of the WSe2/hBN phototransistor (a) [33], $Pb(Zr_{0.2}Ti_{0.8})O_3$-based ferroelectric photodiode (b) [58], WSe2-based lateral photodiode (c) [17] and this work. Device compactness is represented by 1/T, where T is the number of terminals of the device; photoresponsivity range is represented by $|R_{positive}-R_{negative}|$, where $R_{positive}$ and $R_{negative}$ are the maximum positive and negative photoresponsivity, respectively; low operation voltage is represented by $1/|V_{max}|$, where V_{max} is the maximum voltage needed; array fill factor is extracted from the device image with scale bar; fabrication simplicity is ranked according to the requrement 1: Atomic layer deposition and mechanical exfoliation, 2: pulsed laser deposition (PLD), 3: solution processible spin-coating. All the performance merits are then normalized with x/x_{max} to plot the radar chart.

Downloaded from pubs.acs.org/ancac3/article-supplement/5207499/pdf/nn6c07332_si_001/ by PURDUE UNIV user on 28 October 2026

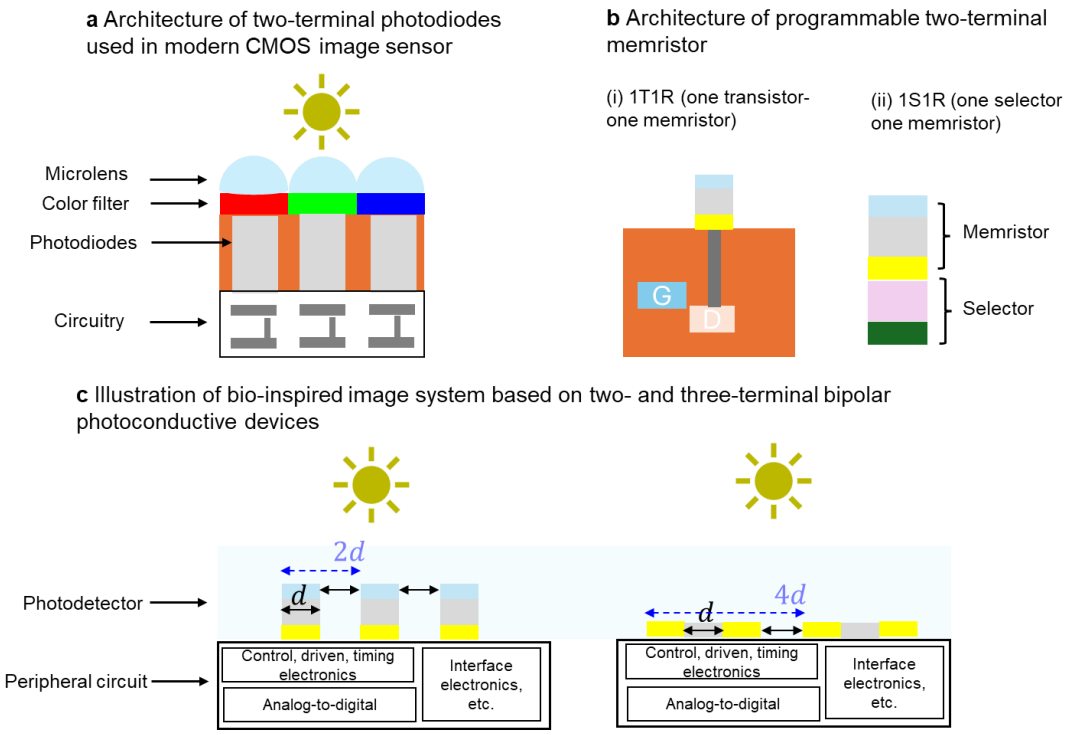

Figure S4. Typical architecture of realizing in-pixel control of two-terminal photodiodes (**a**) and memristor (**b**). **c**, Comparison in the effective photo-sensing area of vertical two-terminal photodetector and phototransistor with lateral sensing channel.

Downloaded from pubs.acs.org/ancac3/article-supplement/5207499/pdf/nn6c07332_si_001/ by PURDUE UNIV user on 28 October 2026

Characterization and working principle of the proposed device

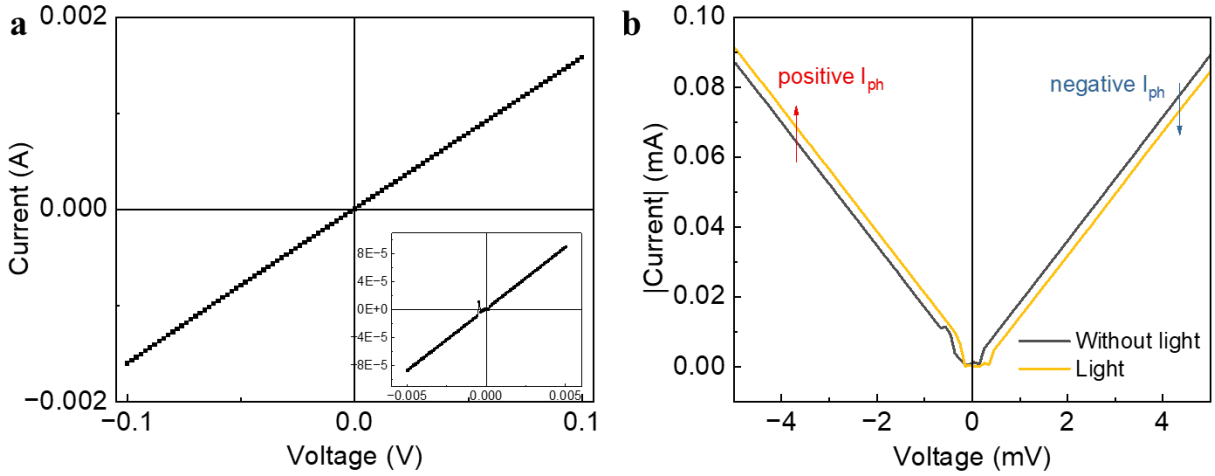

Figure S5. a, IV curve of the ITO/n-PBDF/Au device in room light condition. The inset is the IV curve scanning within ± 5 mV. **b**, IV curve of the device with and without light stimuli (532 nm).

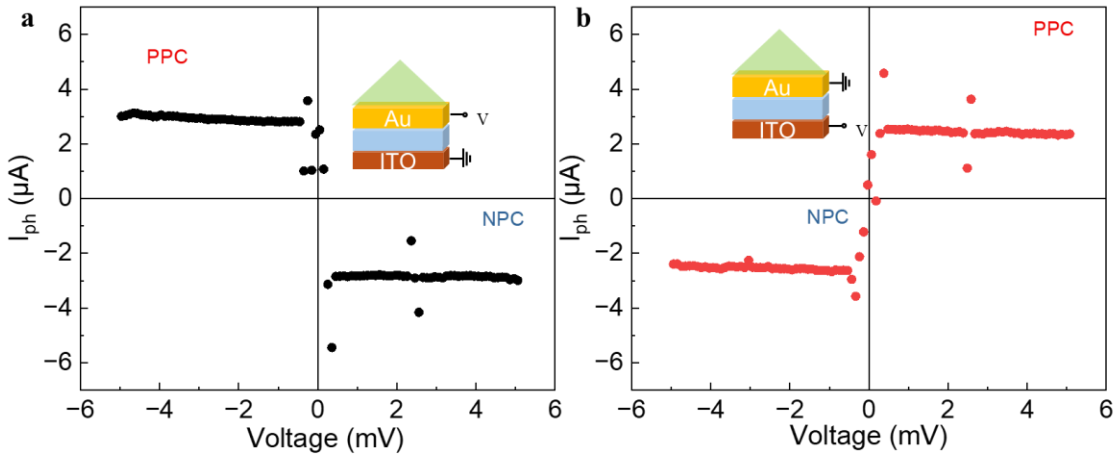

Figure S6. PPC/NPC is programmed by the electric field direction but not the light source direction.

Downloaded from pubs.acs.org/ancac3/article-supplement/5207499/pdf/nn6c07332_si_001/ by PURDUE UNIV user on 28 October 2026

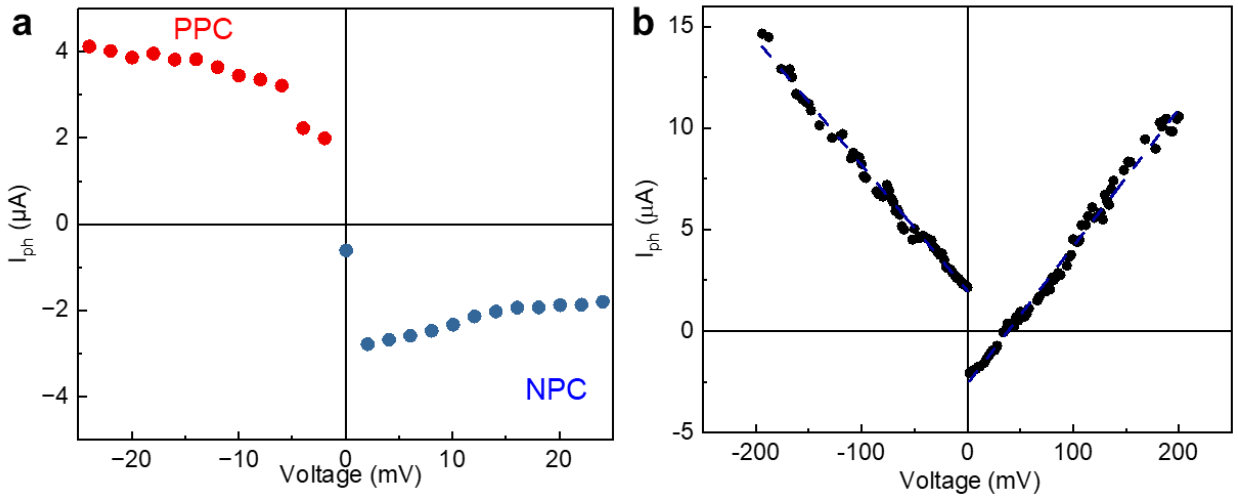

Figure S7. Electrical bias modulated photocurrent of the ITO/n-PBDF/Au device within different voltage scanning range.

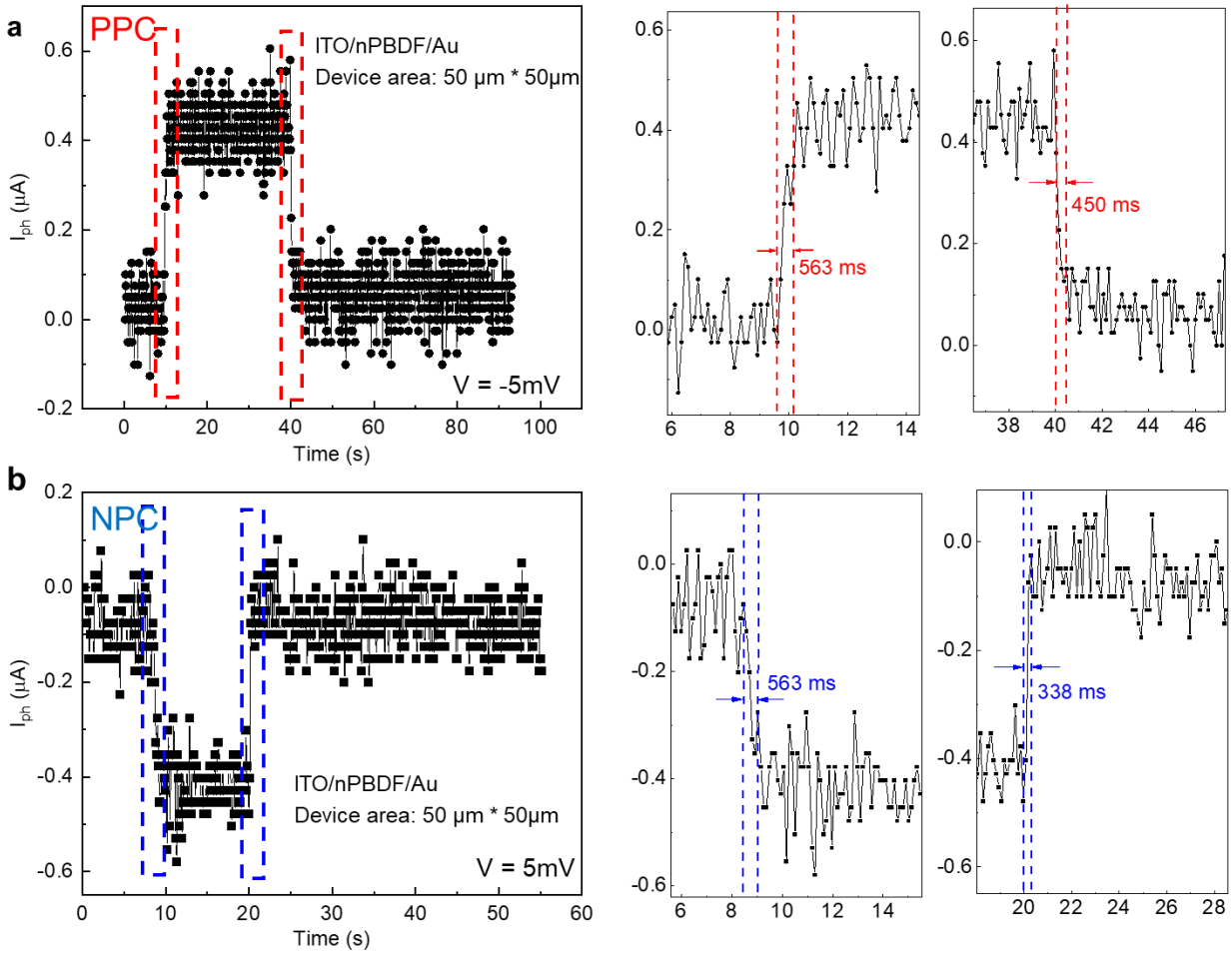

Figure S8. Response and decay time of the device with 50μm*50μm area. **a**, Positive photoresponse when V=-5mV. **b**, Negative photoresponse when V = 5 mV.

Downloaded from pubs.acs.org/ancac3/article-supplement/5207499/pdf/nn6c07332_si_001/ by PURDUE UNIV user on 28 October 2026

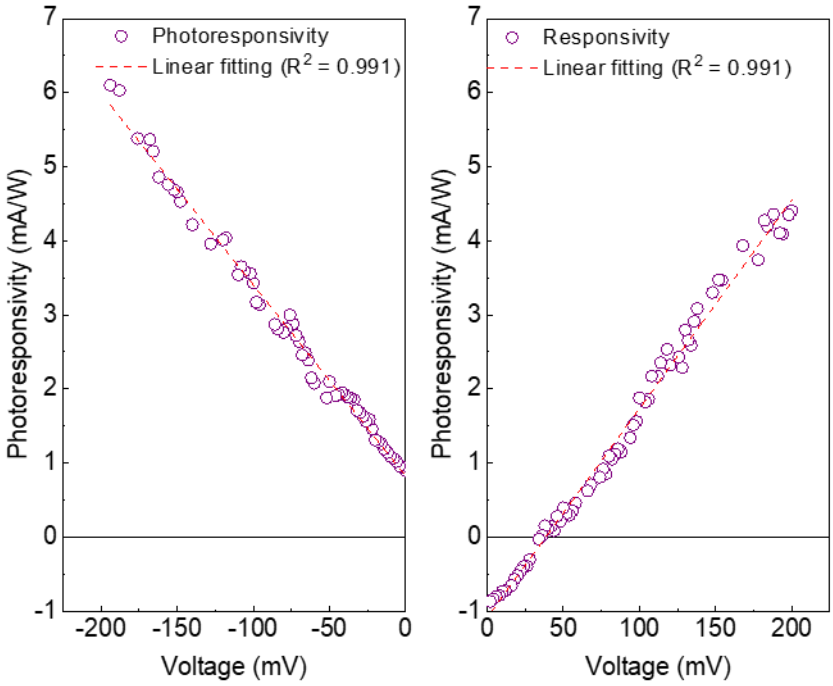

Figure S9. Voltage bias modulated photoresponsivity within ±200 mV under 532nm, 18.98 mW light power.

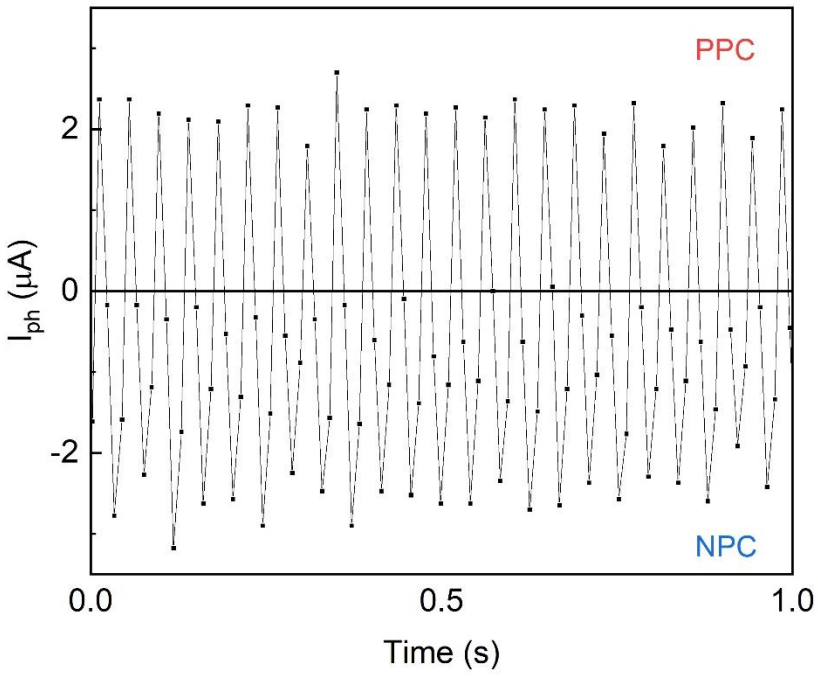

Figure S10. Time-dependent photoresponse switching between PPC and NPC triggered by electrical bias switching between -5 and +5 mV.

Downloaded from pubs.acs.org/ancac3/article-supplement/5207499/pdf/nn6c07332_si_001/ by PURDUE UNIV user on 28 October 2026

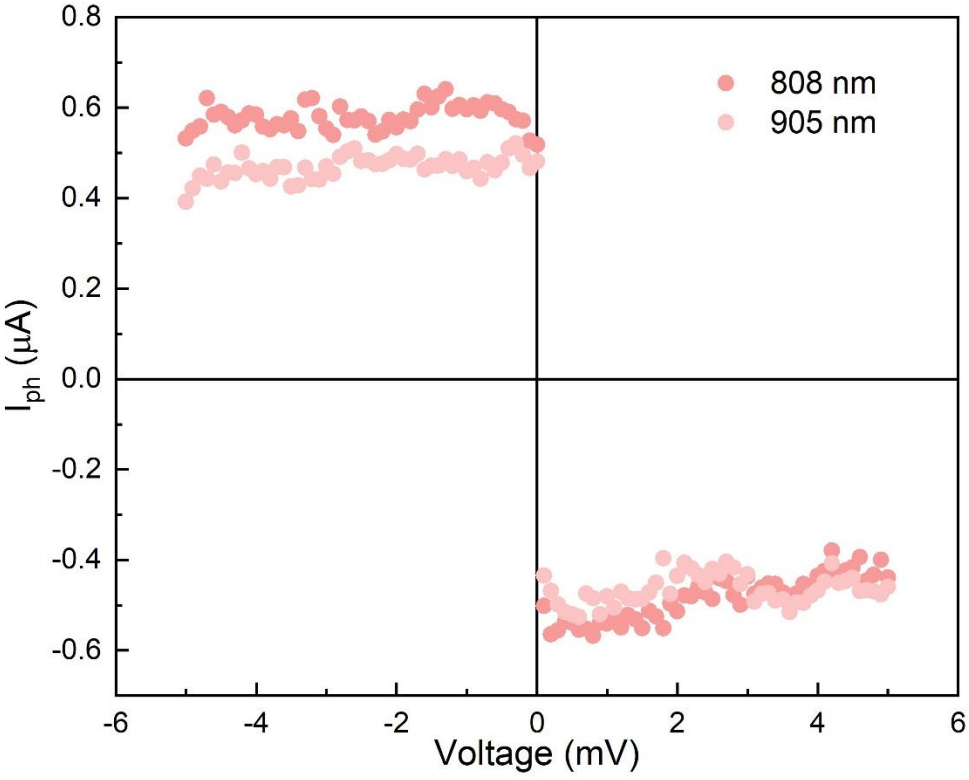

Figure S11. ITO/n-PBDF/Au showing bias-modulated bipolar photoresponse

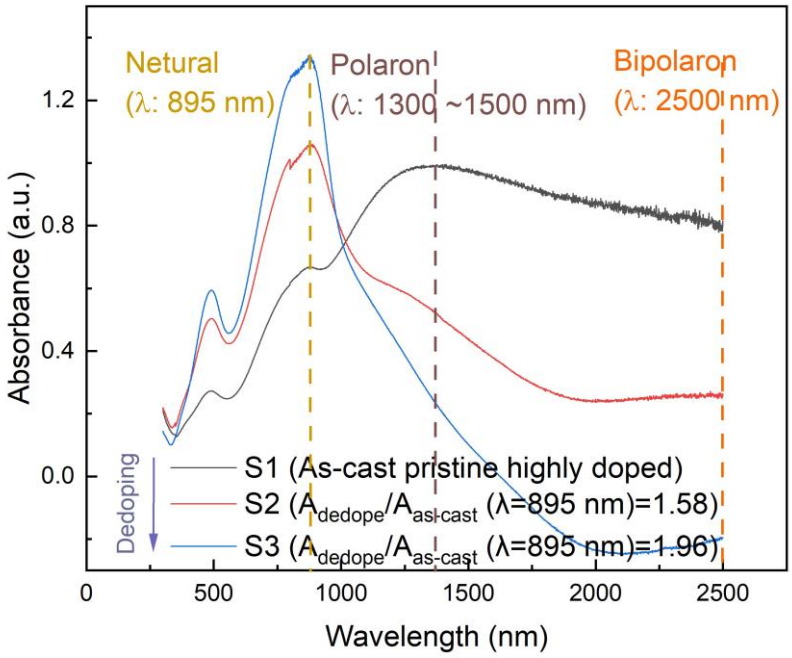

Figure S12. UV-Vis of the samples in Fig. 3A.

Downloaded from pubs.acs.org/ancac3/article-supplement/5207499/pdf/nn6c07332_si_001/ by PURDUE UNIV user on 28 October 2026

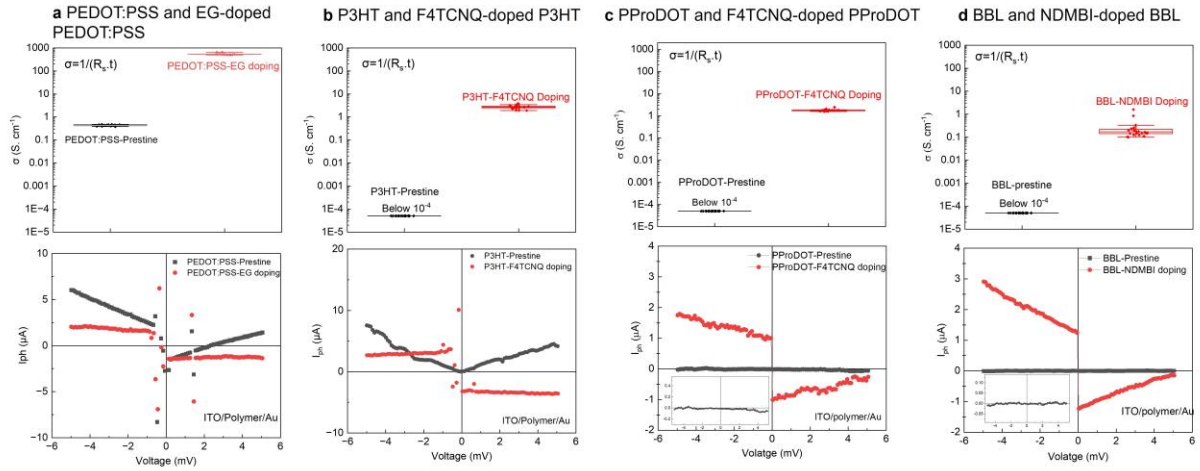

Figure S13. Conductivity (Top) and photoresponse (Bottom) of pristine and chemically doped organic polymers of PEDOT:PSS (**a**), P3HT (**b**), PProDOT (**c**) and BBL (**d**) as the active layer sandwiched between ITO and Au electrodes.

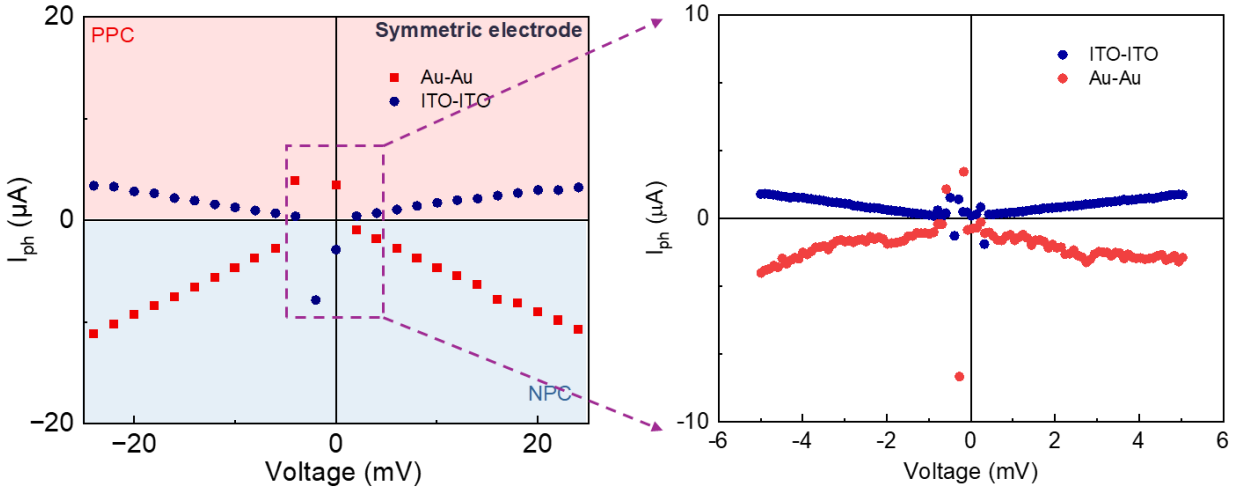

Figure S14. Photoconductivity of symmetric ITO and Au electrode.

Downloaded from pubs.acs.org/ancac3/article-supplement/5207499/pdf/nn6c07332_si_001/ by PURDUE UNIV user on 28 October 2026

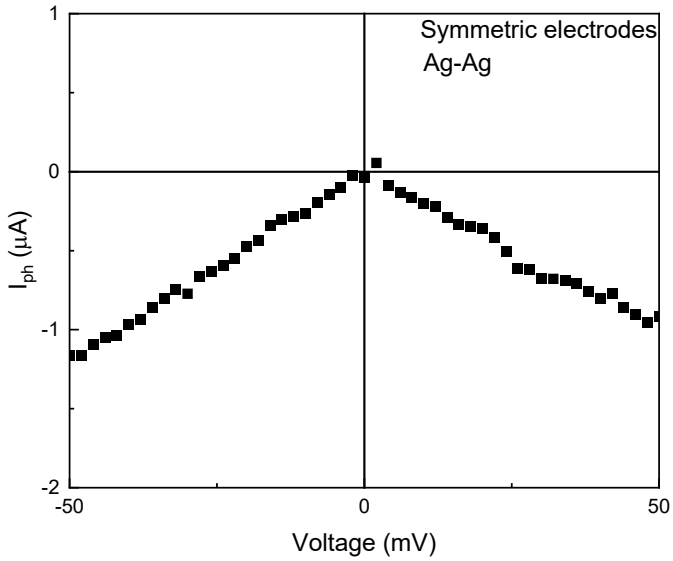

Figure S15. Photoresponse of the device with symmetric electrode of Ag.

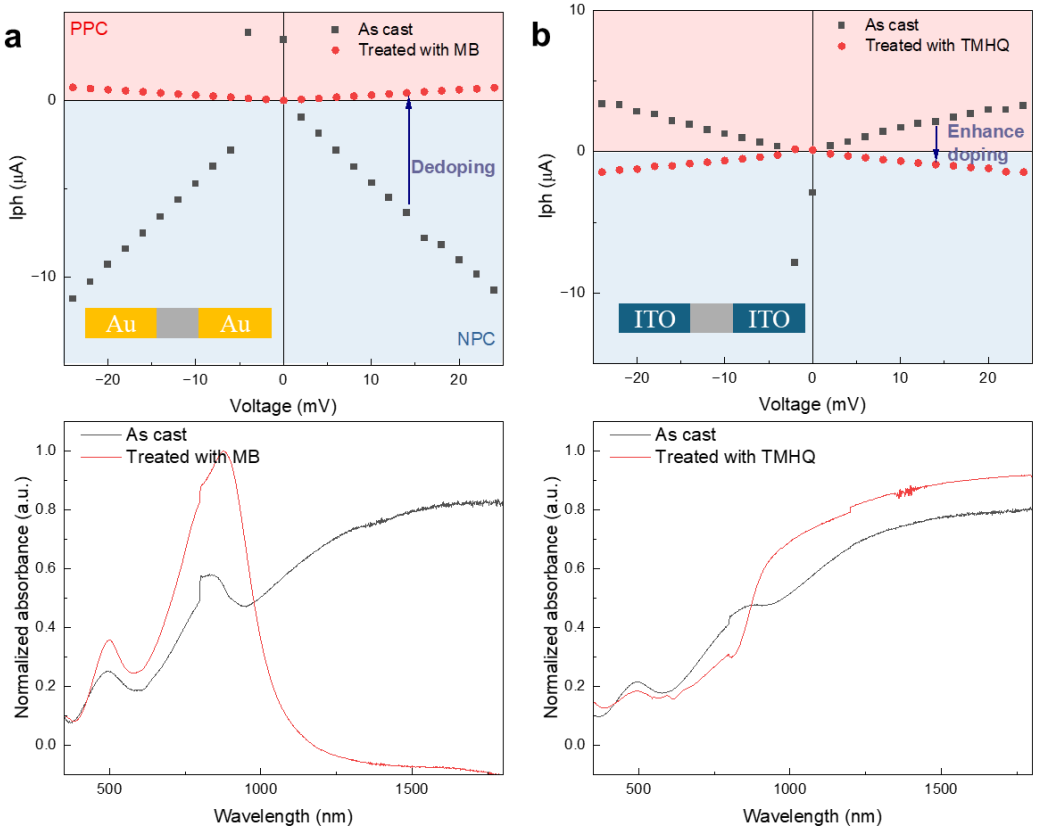

Figure S16. Photoresponses of the symmetric Au (**a**) and ITO (**b**) electrode with different doping levels.

Downloaded from pubs.acs.org/ancac3/article-supplement/5207499/pdf/nn6c07332_si_001/ by PURDUE UNIV user on 28 October 2026

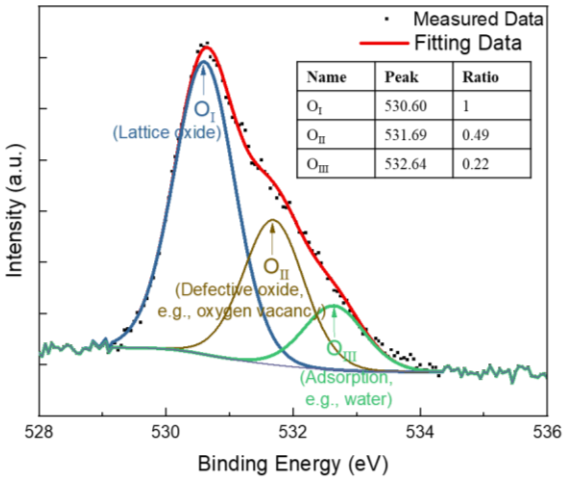

Figure S17. X-ray photoelectron spectroscopy (XPS) of used ITO.

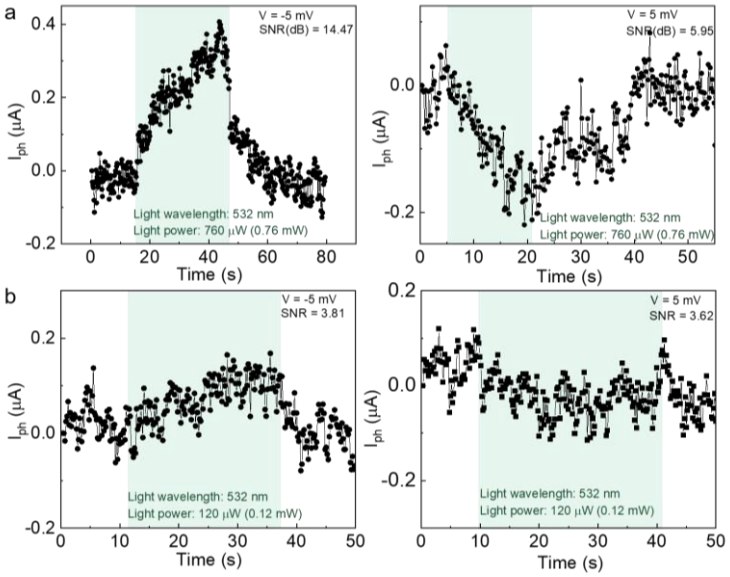

Figure S18. Voltage-modulated bipolar photoresponse of ITO/n-PBDF/Au device under light stimuli of 760 (**a**) and 120 (**b**) μW respectively. Light spot area: 0.15 mm^2.

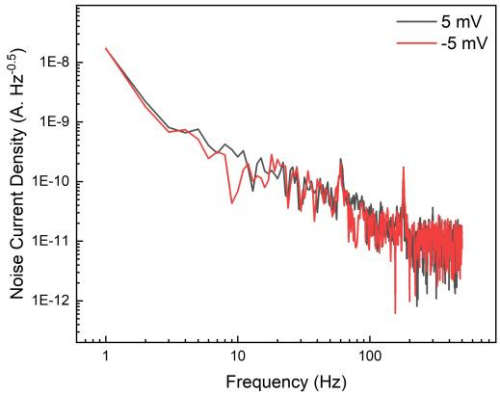

Downloaded from pubs.acs.org/ancac3/article-supplement/5207499/pdf/nn6c07332_si_001/ by PURDUE UNIV user on 28 October 2026

Figure S19. Measurement of noise current of ITO/n-PBDF/Au device

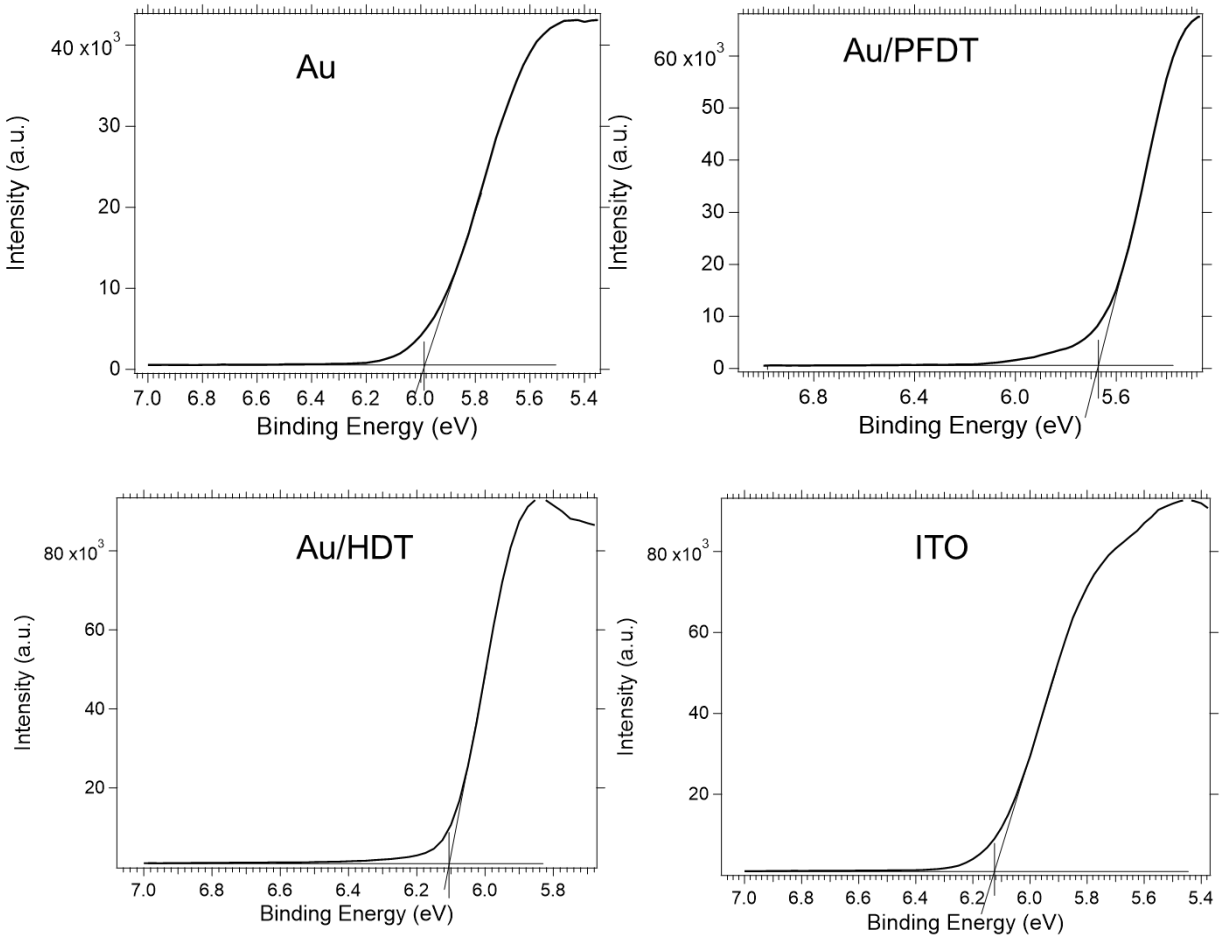

Figure S20. Secondary electron cut-off (SECO) region for the UPS measurement spectrums of Au, Au/PFDT, Au/HDT, and ITO. The WF is calculated as WF = $h\nu$ – SECO, where $h\nu$ is 10.2 eV and the SECO is determined by the intersection of the linear fit of the SECO onset with the background. PFDT: 1H,1H,2H,2H-perfluorodecanethiol. HDT: 1-Hexanethiol.

Downloaded from pubs.acs.org/ancac3/article-supplement/5207499/pdf/nn6c07332_si_001/ by PURDUE UNIV user on 28 October 2026

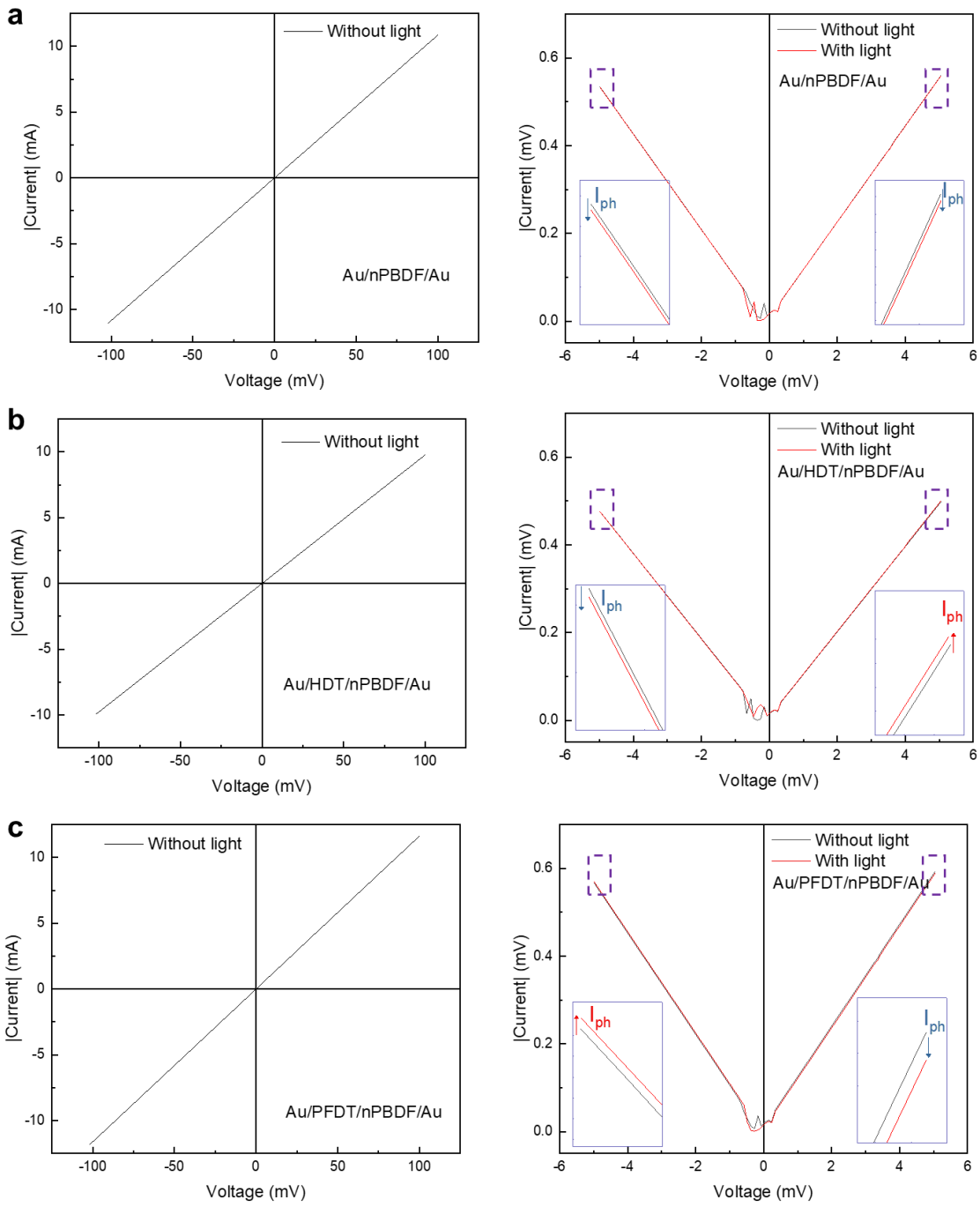

Figure S21. IV curves of (**a**) Symmetric Au electrode without modification. SAM modified electrodes (**b**) Au/HDT and (**c**) Au/PFDT.

Downloaded from pubs.acs.org/ancac3/article-supplement/5207499/pdf/nn6c07332_si_001/ by PURDUE UNIV user on 28 October 2026

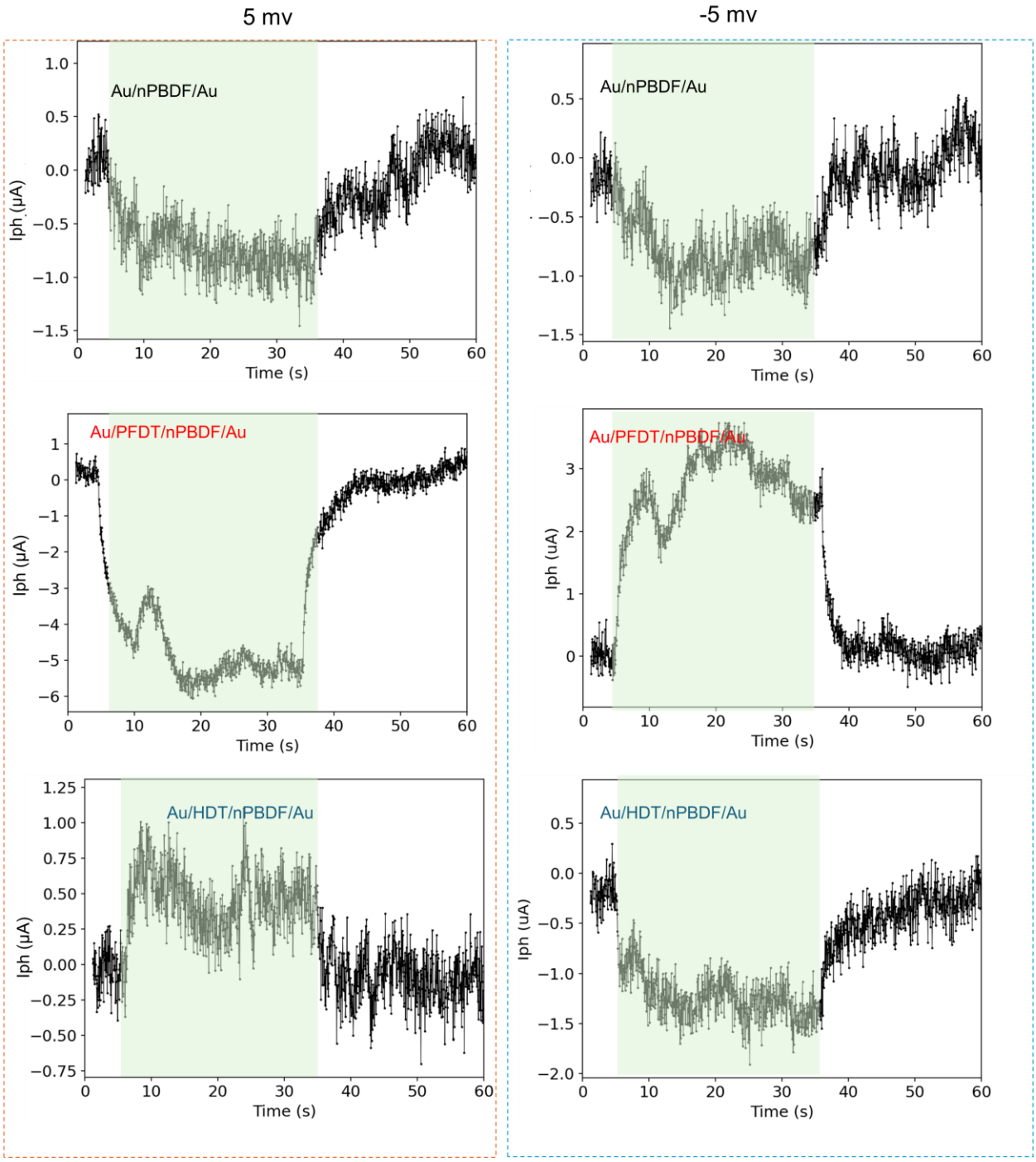

Figure S22. Time-dependent response of the SAM modified Au electrodes at the applied voltages of ± 5mV.

Downloaded from pubs.acs.org/ancac3/article-supplement/5207499/pdf/nn6c07332_si_001/ by PURDUE UNIV user on 28 October 2026

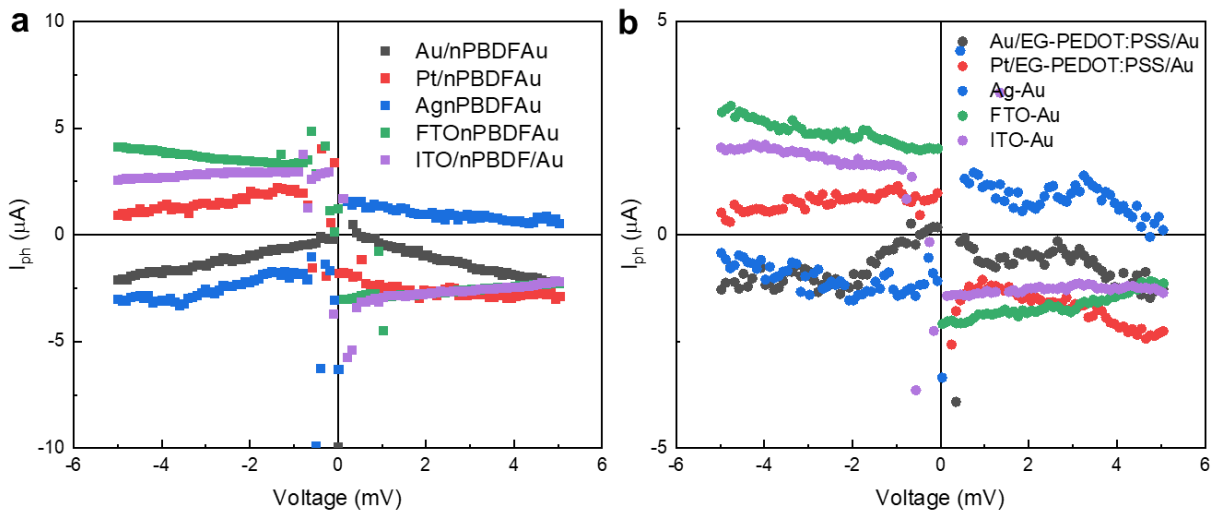

Figure S23. Bipolar photoconductive device with n-PBDF (**a**) and EG-doped PEDOT: PSS (**b**) and various asymmetric electrodes of Au, Pt, Ag, FTO and ITO.

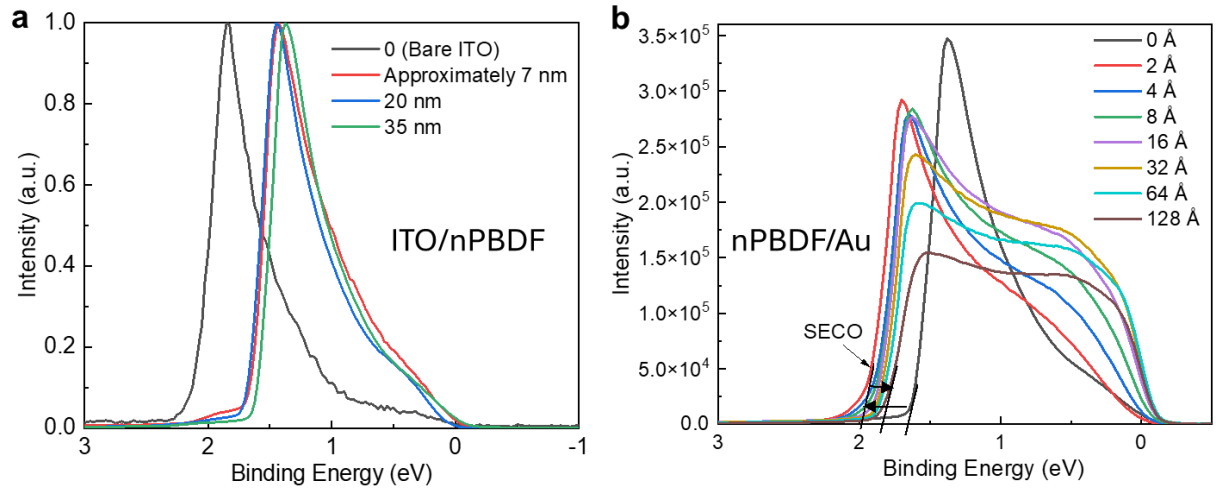

Figure S24. UPS measurement spectrums of n-PBDF with different thickness on ITO substrate (**a**) and thermally deposited Au with different thickness (**b**). The thickness measurement on ITO is limited by the roughness of ITO surface and profilometer detectability.

Downloaded from pubs.acs.org/ancac3/article-supplement/5207499/pdf/nn6c07332_si_001/ by PURDUE UNIV user on 28 October 2026

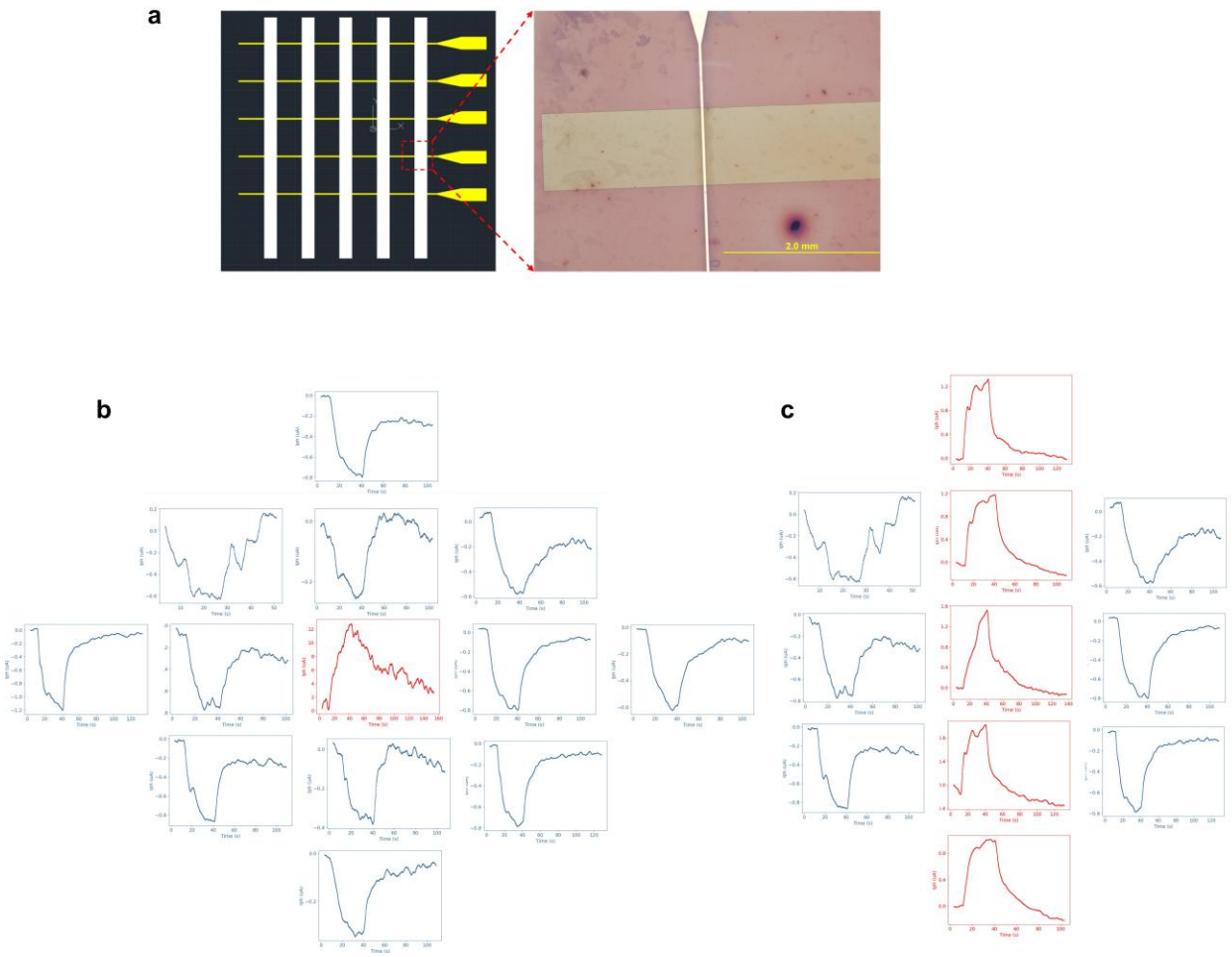

Figure S25. The individual photoresponse to obtain Fig. 4 B, C.

Downloaded from pubs.acs.org/ancac3/article-supplement/5207499/pdf/nn6c07332_si_001/ by PURDUE UNIV user on 28 October 2026

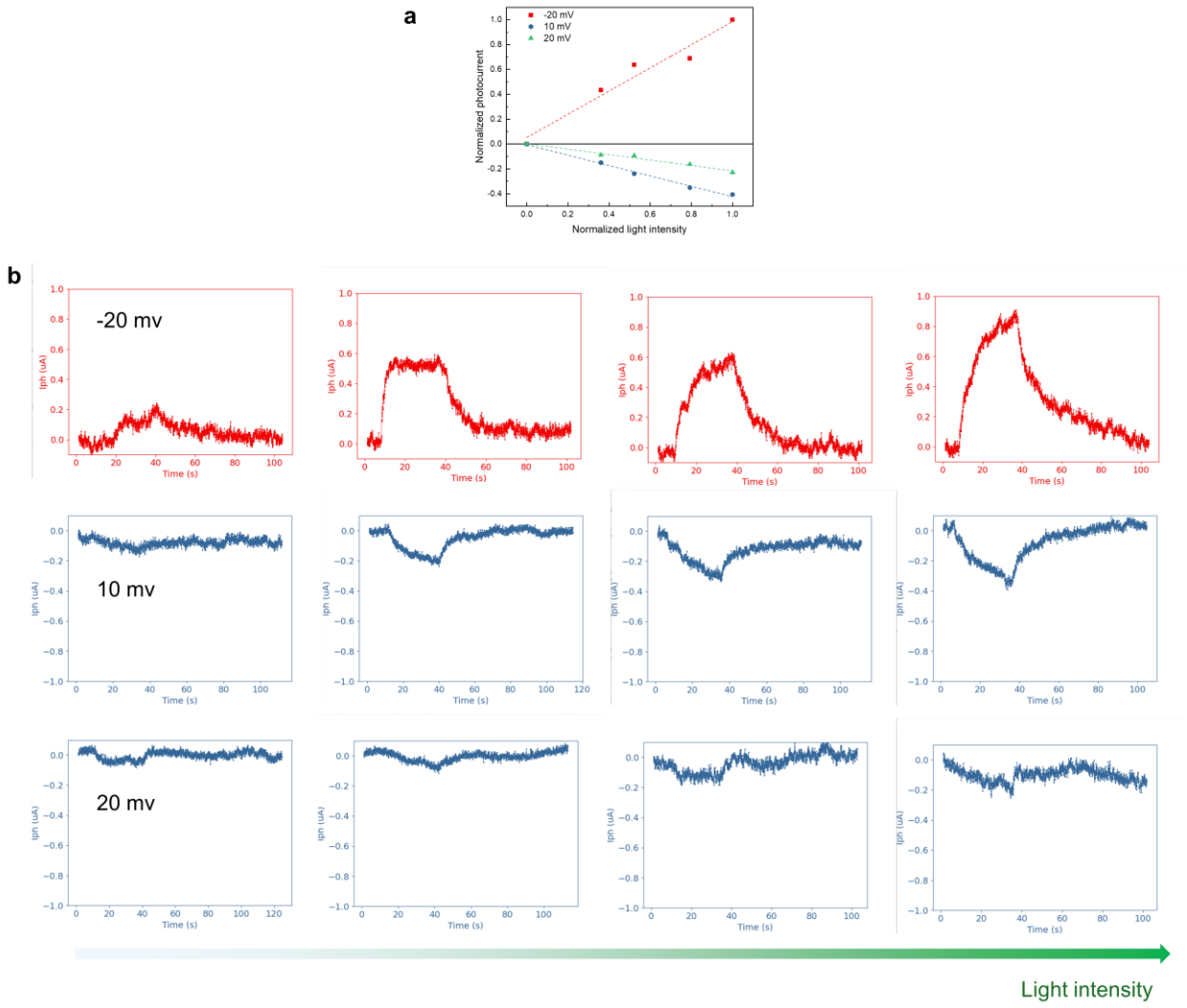

Figure S26. Relationship between light intensity and photocurrent under different bias.

Downloaded from pubs.acs.org/ancac3/article-supplement/5207499/pdf/nn6c07332_si_001/ by PURDUE UNIV user on 28 October 2026

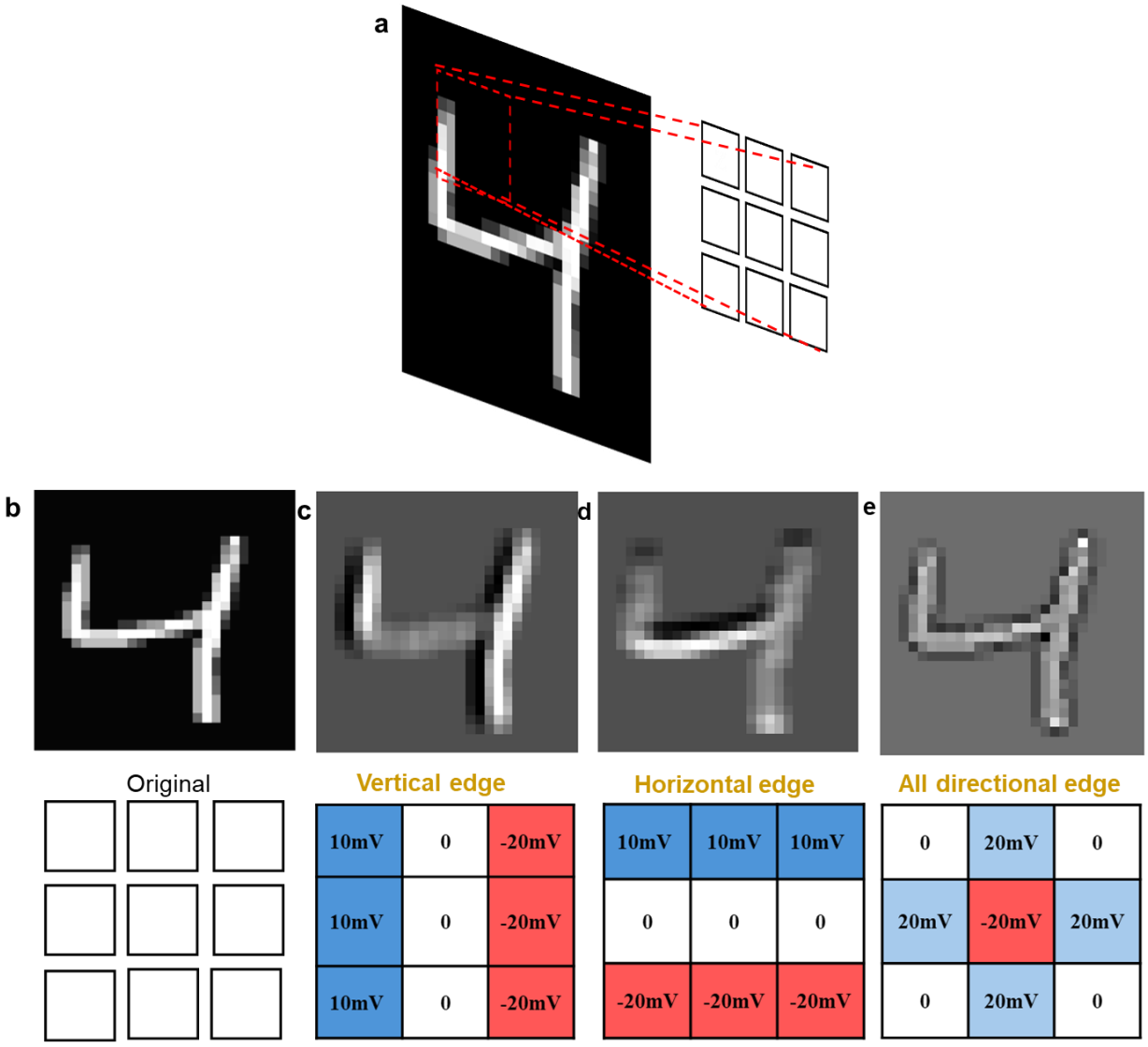

Figure S27. Simulations of different image processing functions with hardware kernels by applying different voltages.

Downloaded from pubs.acs.org/ancac3/article-supplement/5207499/pdf/nn6c07332_si_001/ by PURDUE UNIV user on 28 October 2026

Sensor array and fingerprint minutiae extraction with in-sensor processing

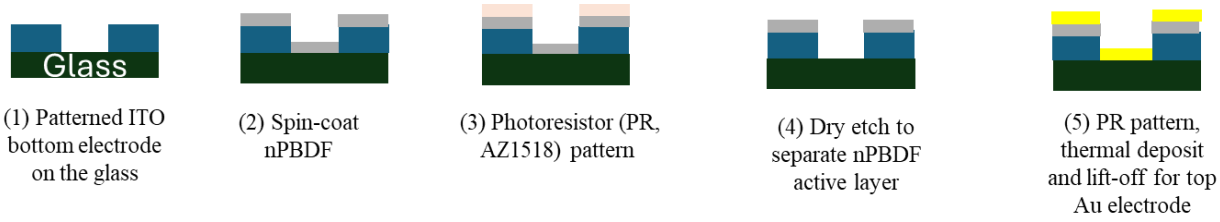

Figure S28. Fabrication process of the array on glass substrate.

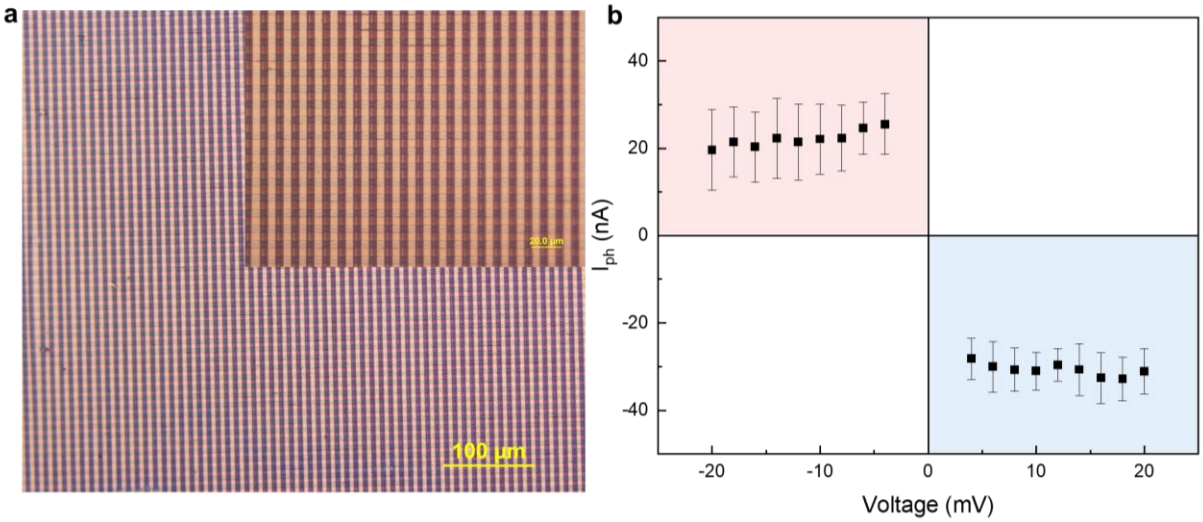

Figure S29. Device array with pitch size of 10 μm. **a**, Optical image. **b**, Bipolar photoresponse of the pixel. Average form eight different pixels.

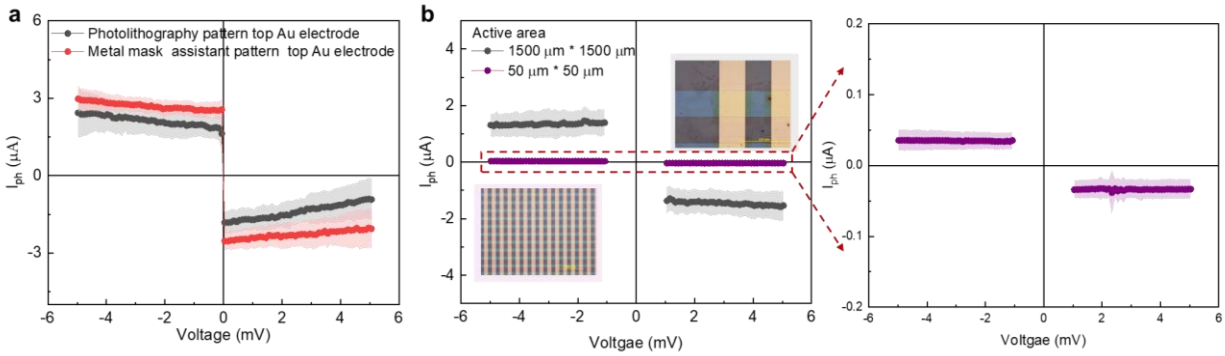

Figure S30. **a,** Comparison of bipolar photoresponse of the device of the top Au electrode patterned via photolithography method and metal shadow mask. **b**, Effect of the active area on the photocurrent of the device.

Downloaded from pubs.acs.org/ancac3/article-supplement/5207499/pdf/nn6c07332_si_001/ by PURDUE UNIV user on 28 October 2026

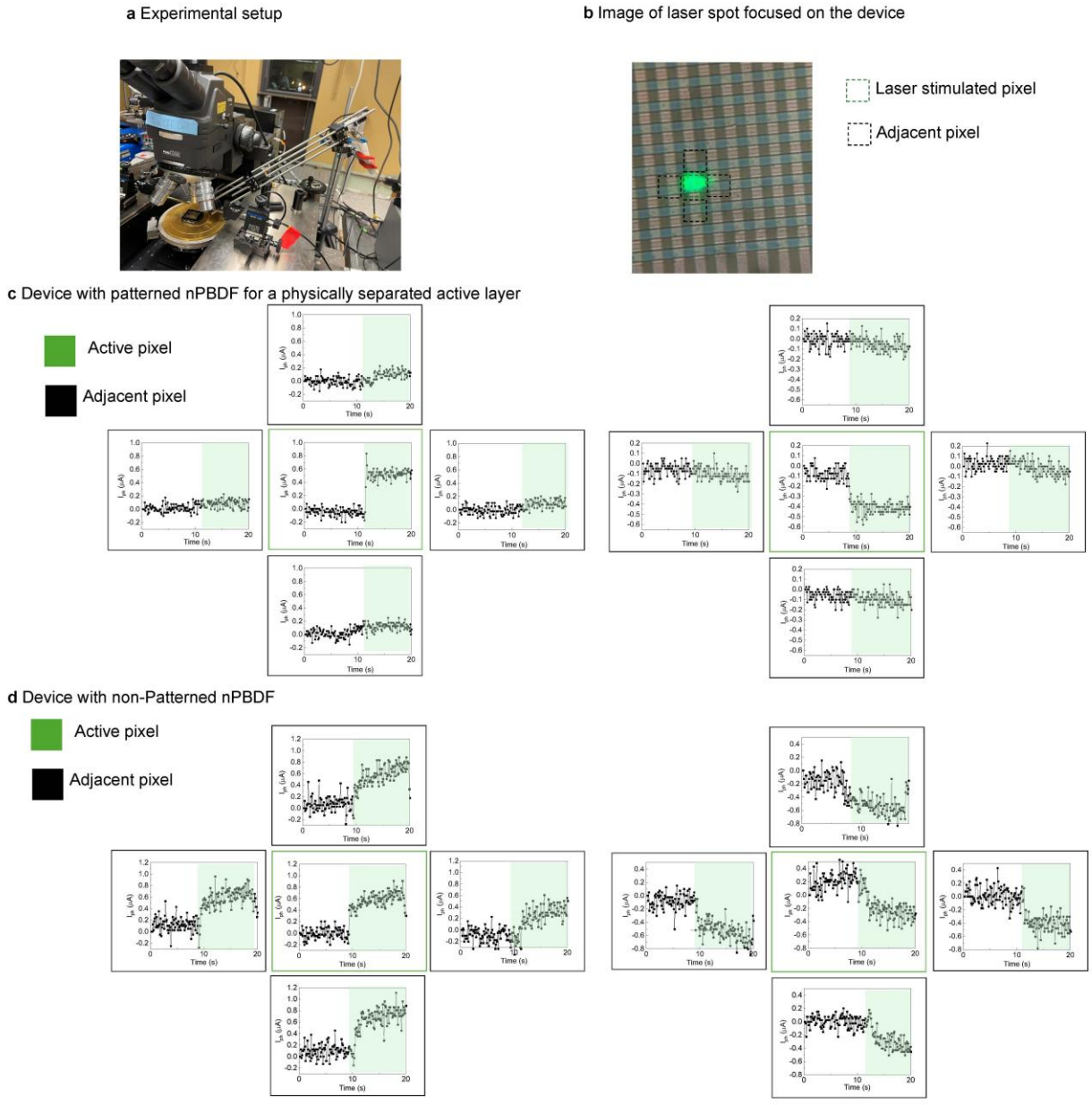

Figure S31. Crosstalk measurement with and without the active layer of n-PBDF patterned. **a**, Experiment setup. **b**, Microscopic image of laser spot on the array pixel. Photoresponse of the active pixel and four adjacent pixels in the device with n-PBDF active layer patterned (**c**) and non-patterned (**d**).

Downloaded from pubs.acs.org/ancac3/article-supplement/5207499/pdf/nn6c07332_si_001/ by PURDUE UNIV user on 28 October 2026

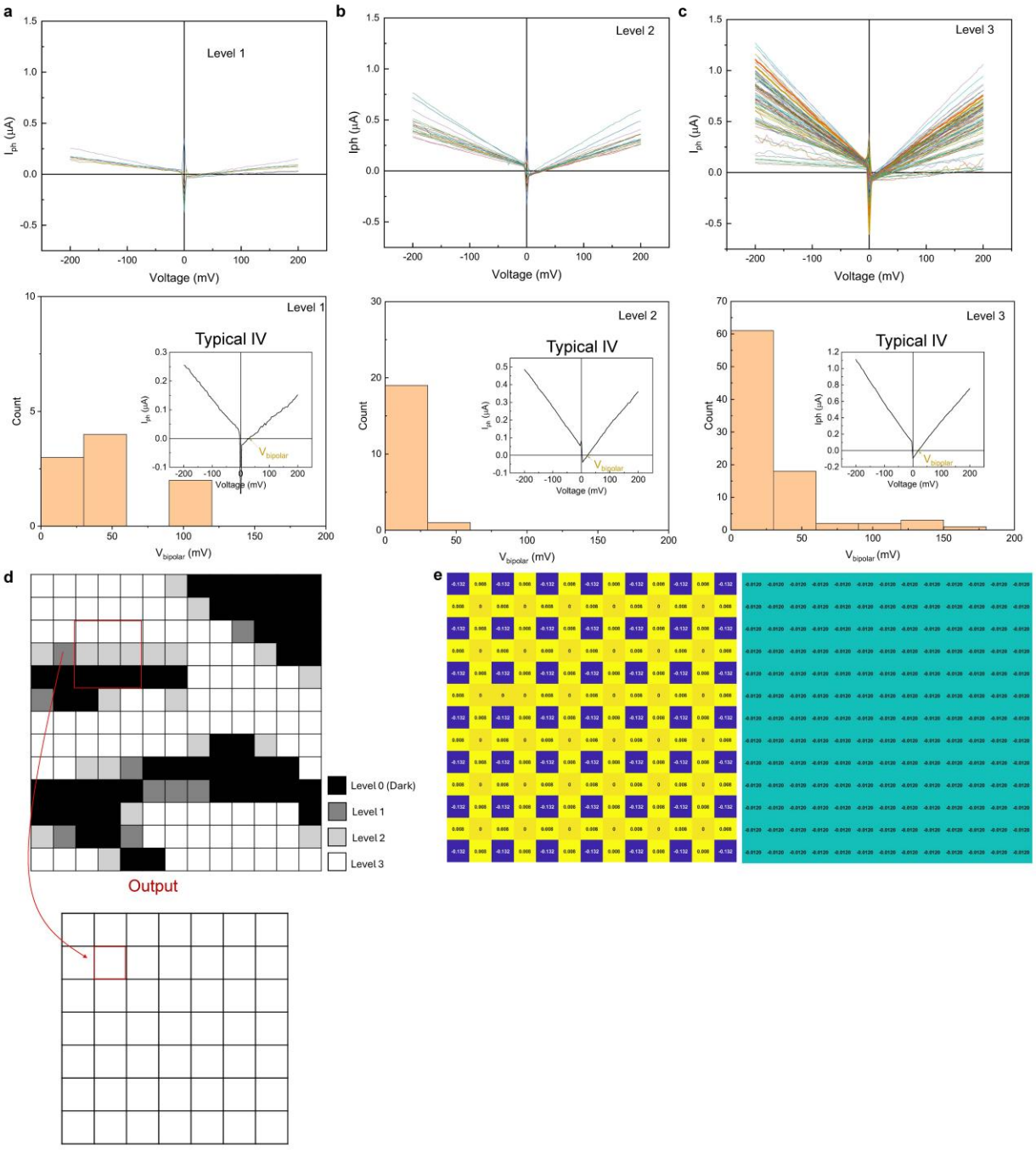

Figure S32. Data used for obtaining the in-sensor edge enhancement fingerprint image. The device output under different stimulation light powers (**a**, **b**, **c**) (Top: Relationship of the output photocurrent and the applied bias, Bottom: Threshold voltage of the photocurrent transits from NPC to PPC; Inset: A typical I_{ph}-V relationship of the pixel under certain light illumination condition.) **d**, Top: The distribution of the four different stimulation light power on each pixel in the 13×13 images. Bottom: Output image with the in-sensor convolution computation result. **e**, The applied bias of each pixel to obtain the output current. (Left: Laplacian kernel for in-sensor edge enhancement. Right: Average kernel without in-sensor edge enhancement). Light stimulation: Level 0: Dark, 53 pixels; Level 1: 12.5mW, 87 pixels; Level 2: 18.98mW, 20 pixels; Level 3: 23.95mW, 9 pixels.

Downloaded from pubs.acs.org/ancac3/article-supplement/5207499/pdf/nn6c07332_si_001/ by PURDUE UNIV user on 28 October 2026

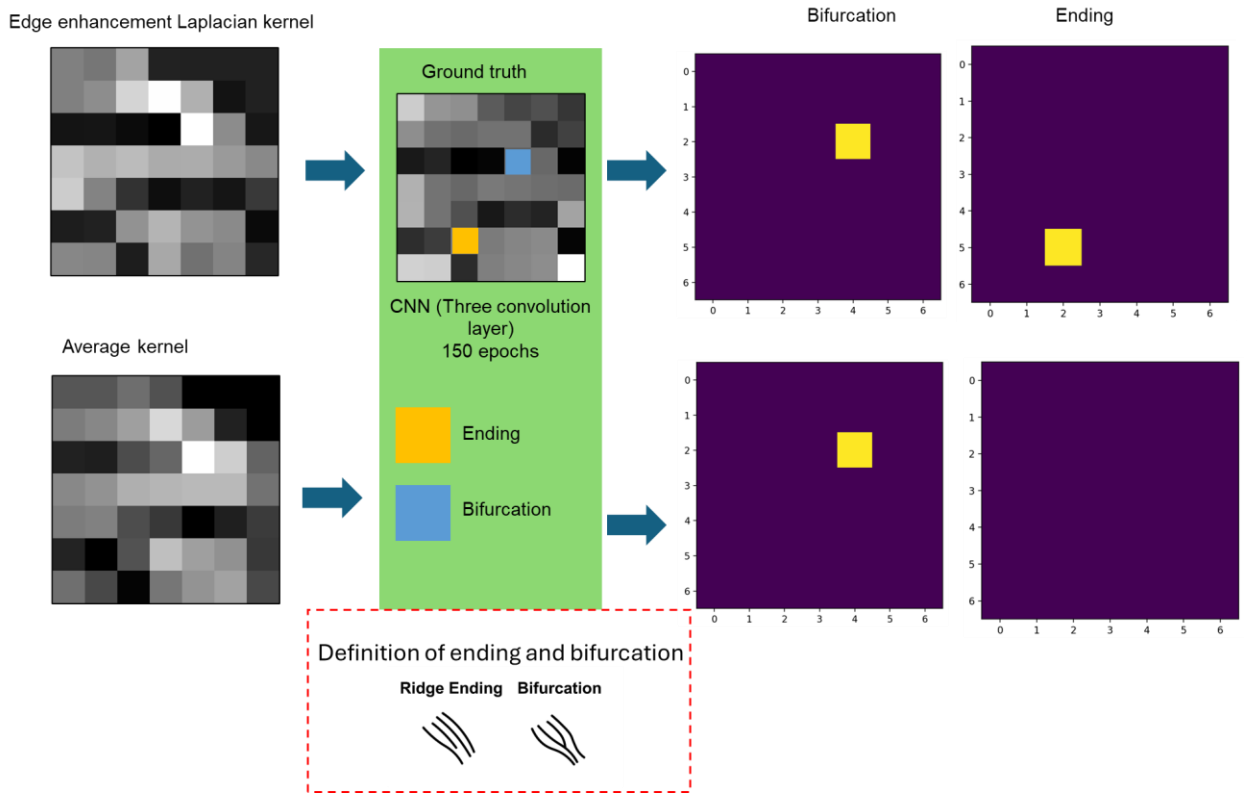

Figure S33. Fingerprint minutiae recognition with the input image sensing with and without edge enhancement kernels.

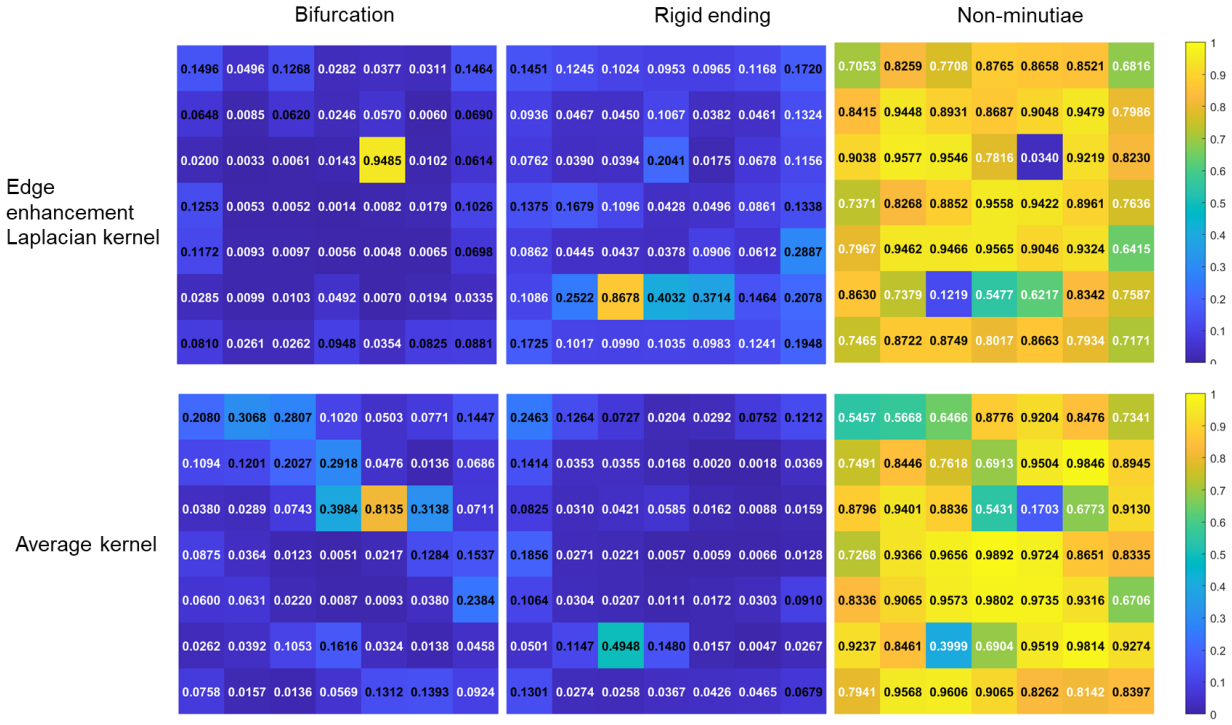

Figure S34. The detailed per-pixel recognition accuracy for bifurcation, ridge ending, and non-minutiae classes in the output image.

Downloaded from pubs.acs.org/ancac3/article-supplement/5207499/pdf/nn6c07332_si_001/ by PURDUE UNIV user on 28 October 2026

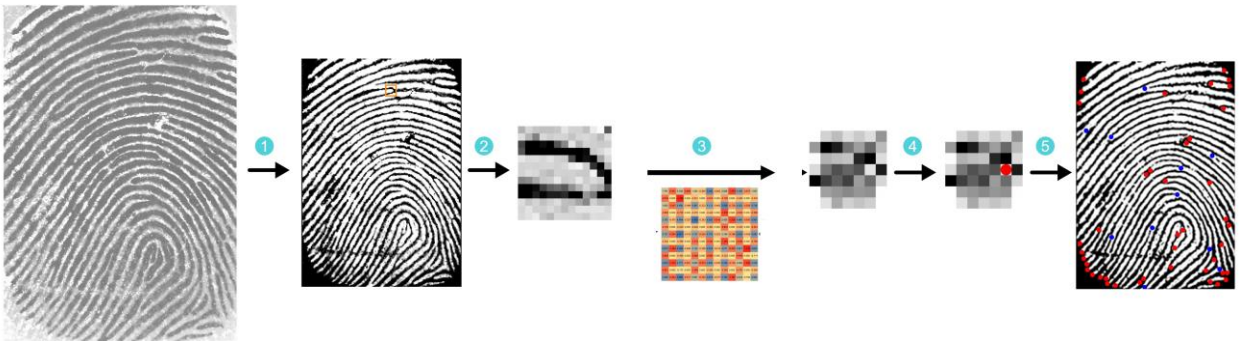

Figure S35. Process simulation to the whole fingerprint image via the cropped image. Step 1: Image inversion and scaling. Step 2: Segmentation into 13 × 13 sub-images. Step 3: Convolution with three predefined kernels. Step 4: Pre-trained CNN-based minutiae prediction. Step 5: Stitching of predicted minutiae.

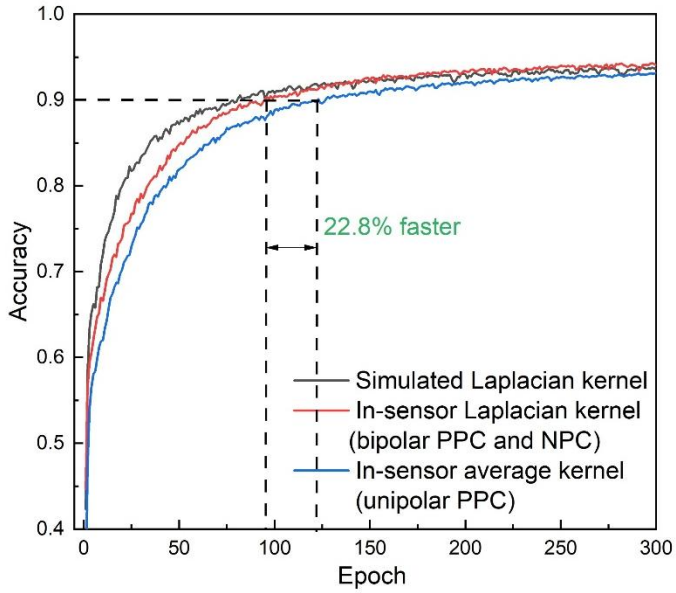

Figure S36. Fingerprint minutiae extraction efficiency using different input images with different kernels.

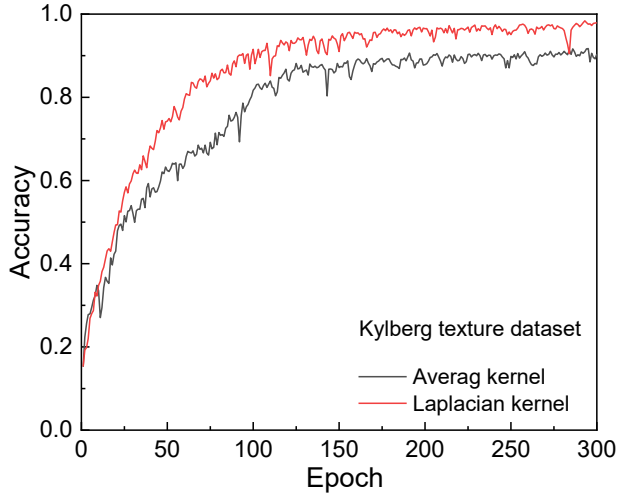

Figure S37. Effect of in-sensor Laplacian kernel on Kylberg texture dataset.

Downloaded from pubs.acs.org/ancac3/article-supplement/5207499/pdf/nn6c07332_si_001/ by PURDUE UNIV user on 28 October 2026

Flexible device fabrication and its functionality

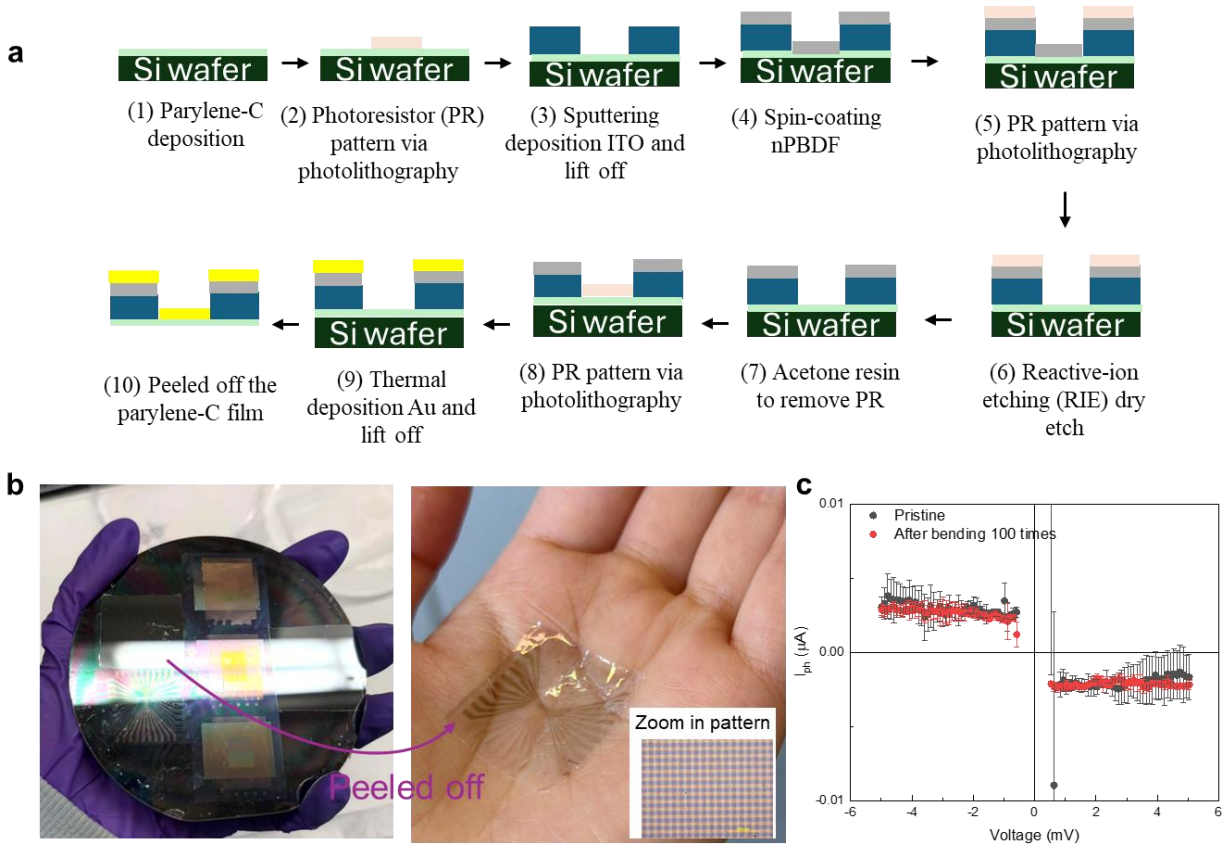

Figure S38. Fabrication process and functionality of flexible sensor with parylene-C substrate. **a**, Mainstream semiconductor processing compatible fabrication process consists of spin-coating, photolithography, sputtering/thermal deposition and dry-etching. **b**, Image of the devices on 4in wafer. **c**, Device bias-modulated bipolar photoconductive functionality before and after bending.

Downloaded from pubs.acs.org/ancac3/article-supplement/5207499/pdf/nn6c07332_si_001/ by PURDUE UNIV user on 28 October 2026

Hardware neural network on crossbar for in-sensor discrimination

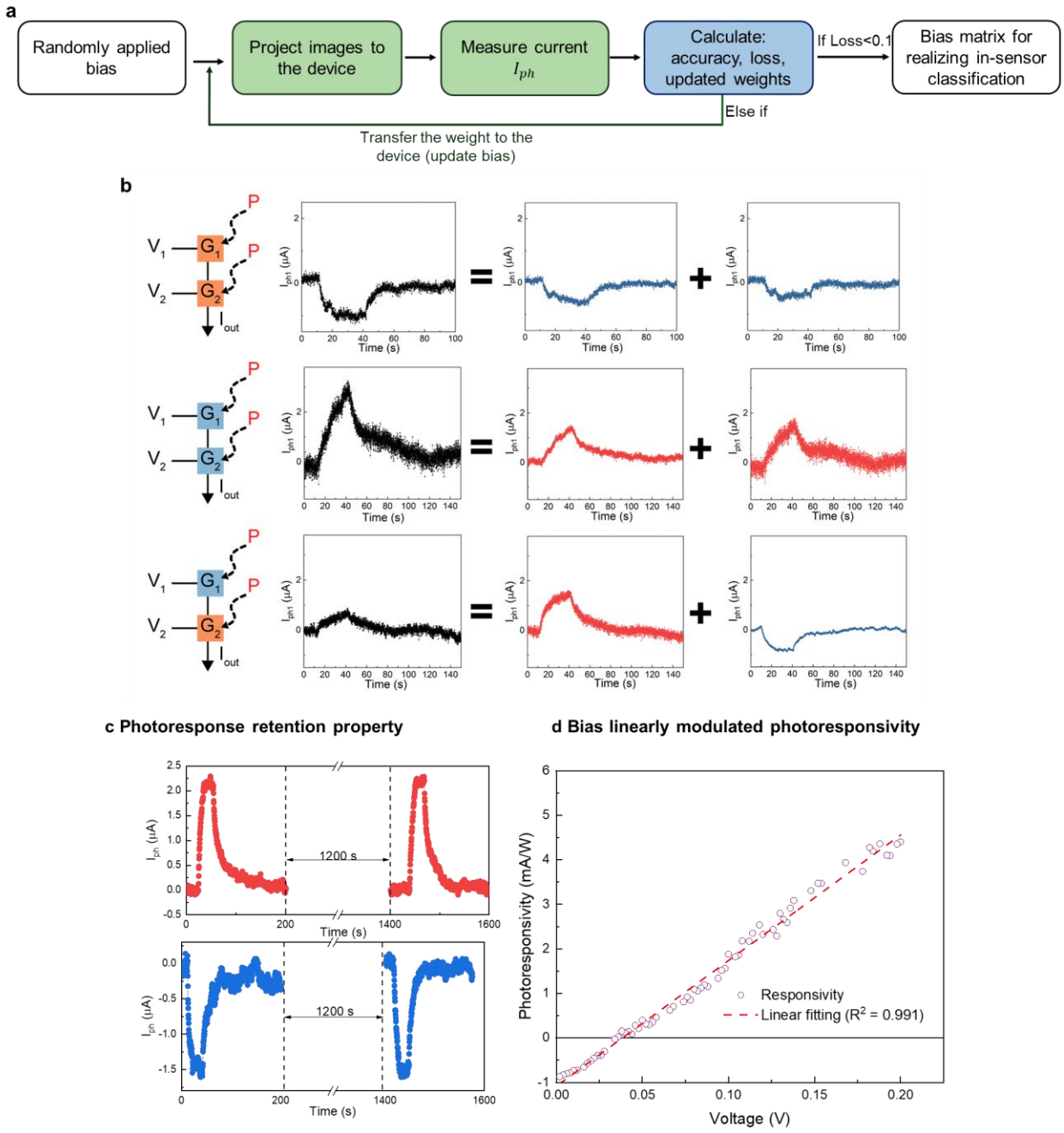

Figure S39. **a**, Flow chart of implementing in-sensor image recognition. **b**, Time-resolved measured photocurrent with combination of different voltage modulated photoresponse on different pixels obeying kirchhoff's law. **c**, photoresponsivity retention of the proposed device. **d**, Bias-modulated photoresponsivity.

Downloaded from pubs.acs.org/ancac3/article-supplement/5207499/pdf/nn6c07332_si_001/ by PURDUE UNIV user on 28 October 2026

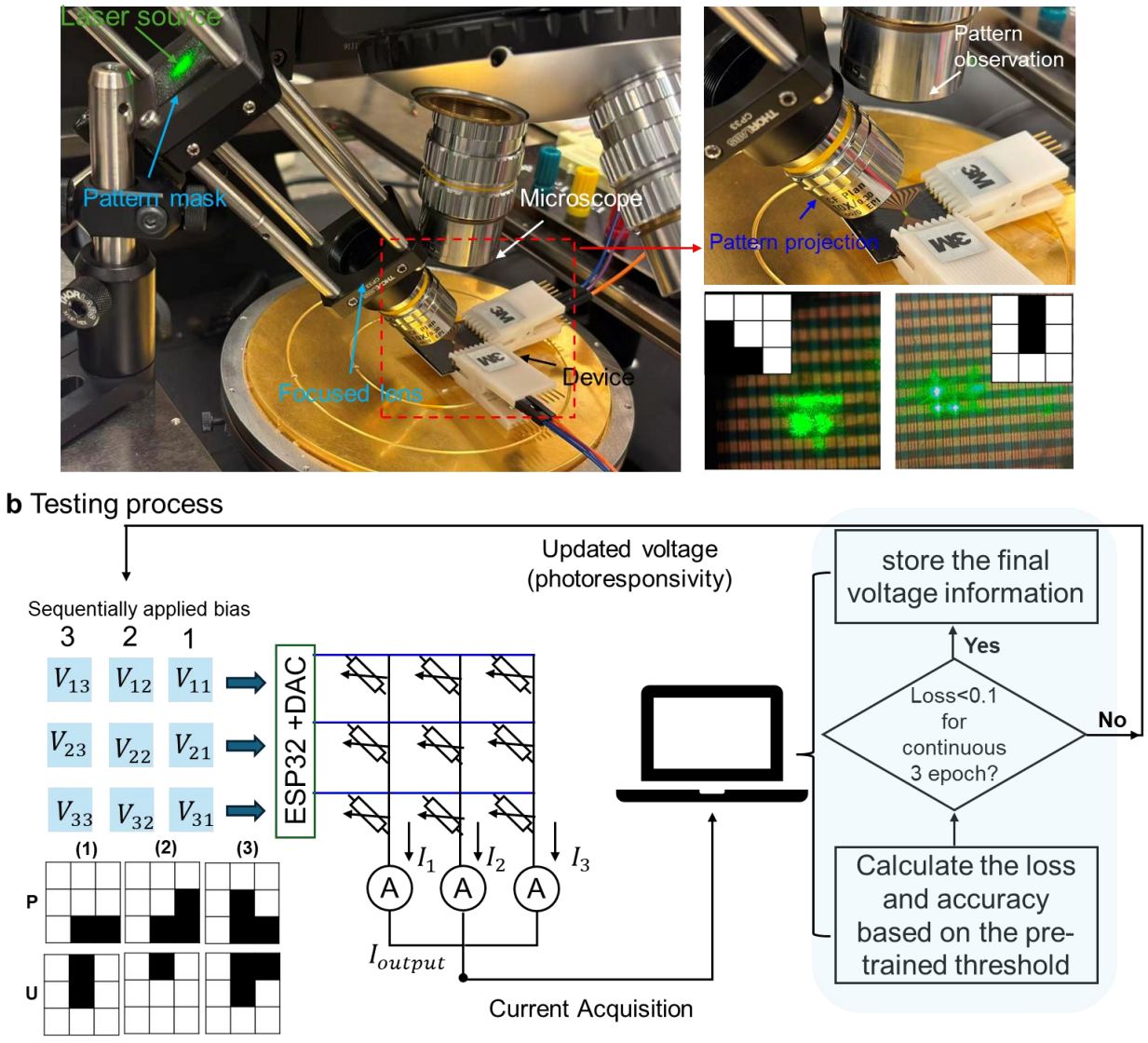

Figure S40. Experimental set up (**a**) and testing process (**b**) of in-sensor pattern recognition.

Downloaded from pubs.acs.org/ancac3/article-supplement/5207499/pdf/nn6c07332_si_001/ by PURDUE UNIV user on 28 October 2026

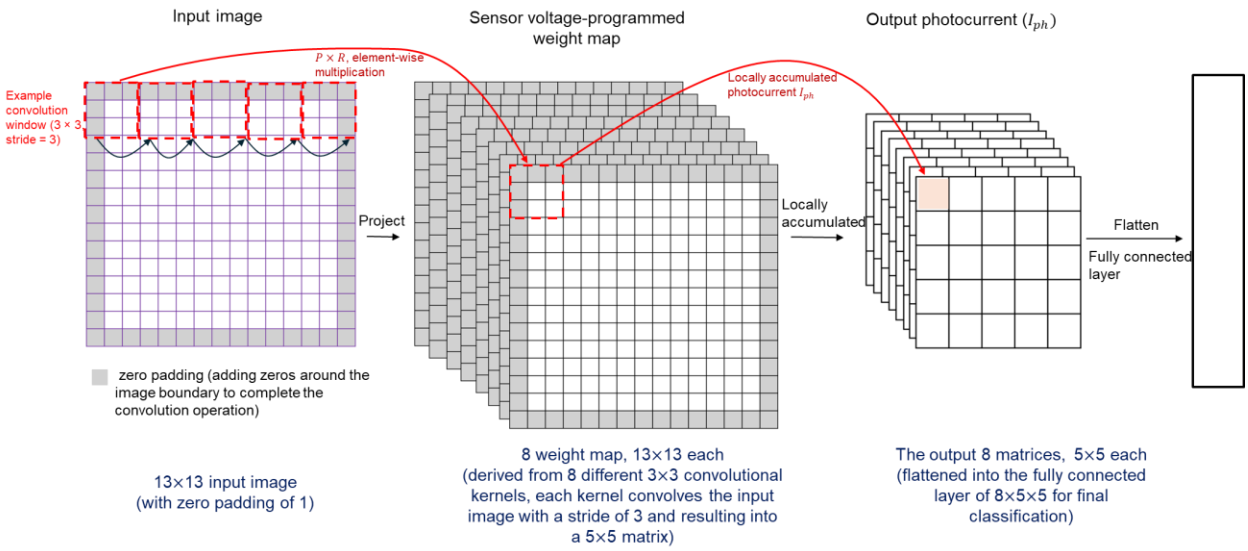

Figure S41. Schematic illustration of the in-sensor convolution operation by implementing neural network on the two-terminal crossbar.

Downloaded from pubs.acs.org/ancac3/article-supplement/5207499/pdf/nn6c07332_si_001/ by PURDUE UNIV user on 28 October 2026

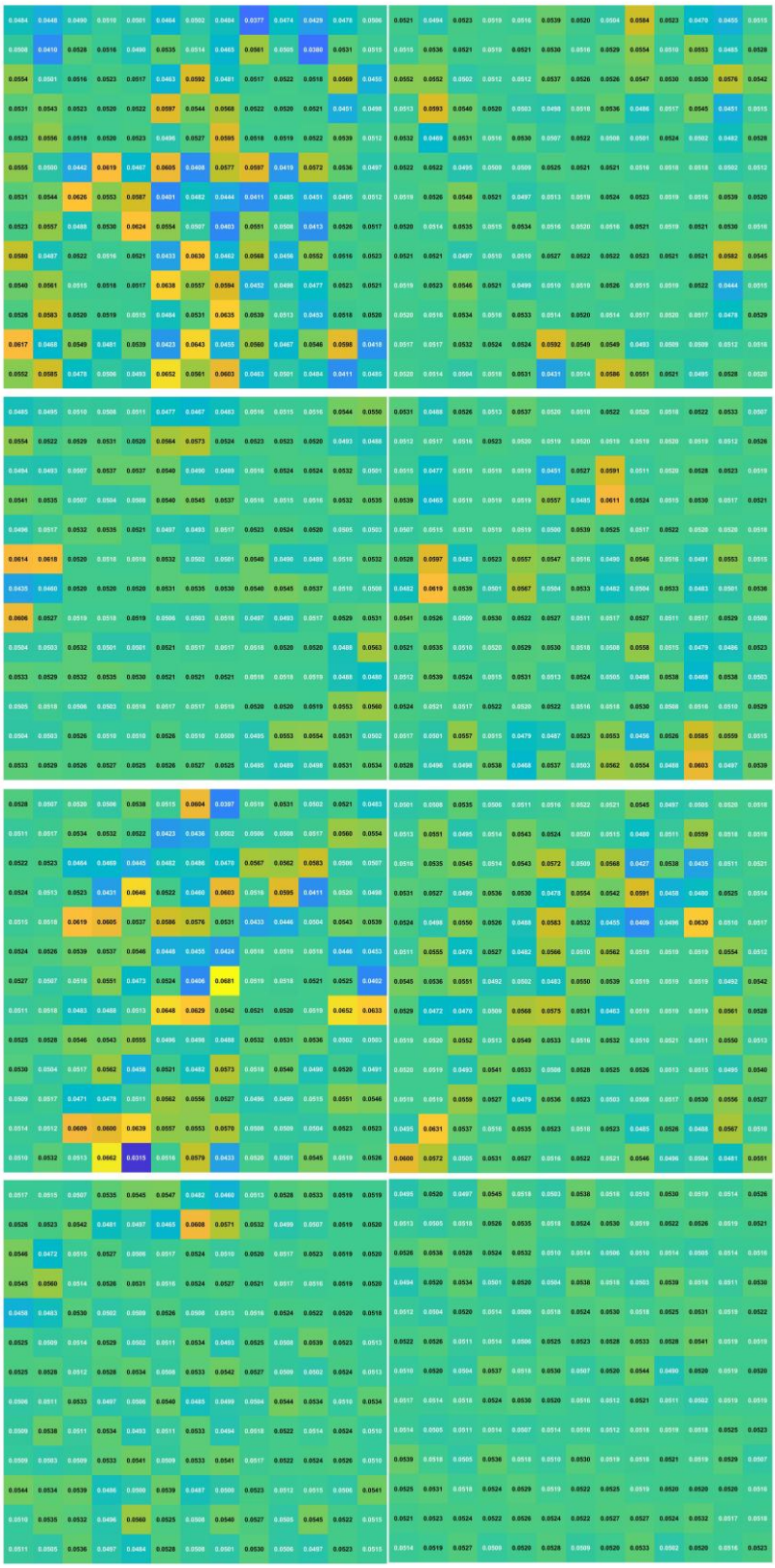

Figure S42. Voltage values to construct the eight different convoluted kernels

Downloaded from pubs.acs.org/ancac3/article-supplement/5207499/pdf/nn6c07332_si_001/ by PURDUE UNIV user on 28 October 2026

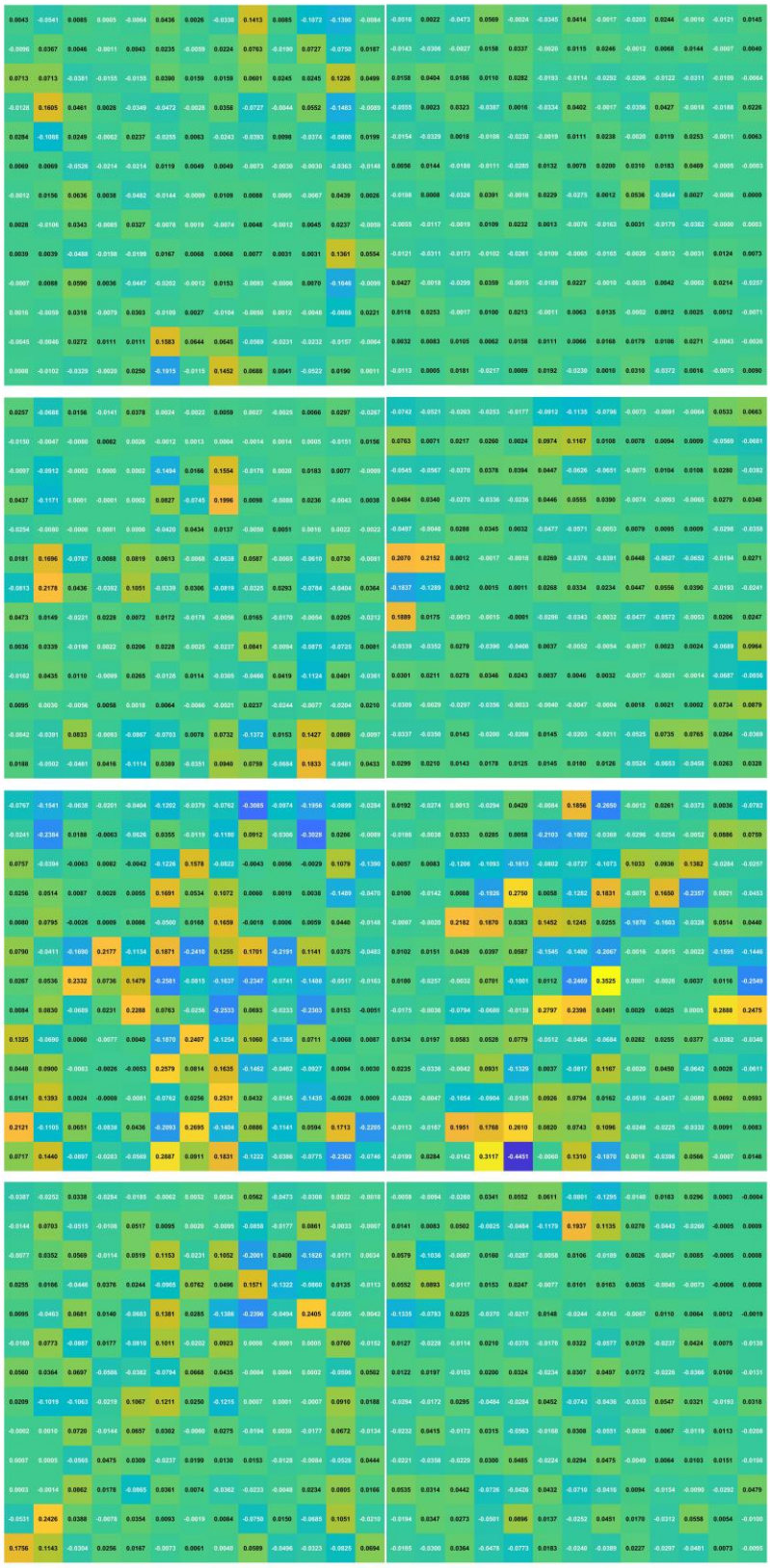

Figure S43. Weight of eight different kernels determined by the applied voltages.

Downloaded from pubs.acs.org/ancac3/article-supplement/5207499/pdf/nn6c07332_si_001/ by PURDUE UNIV user on 28 October 2026

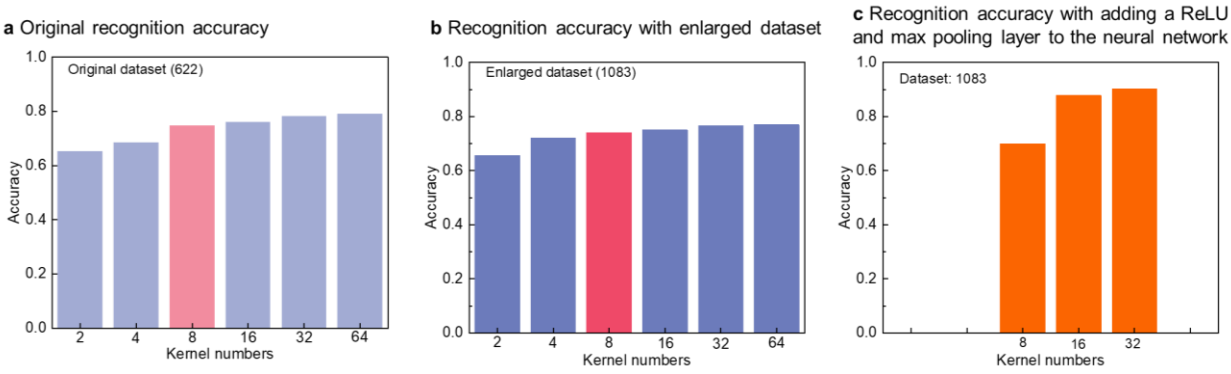

Figure S44. Analysis of the recognition accuracy of hardware neural network. Recognition accuracy of the original dataset consists of 622 images with a convolutional and a fully connection layer (**a**), enlarged dataset of 1083 images (**b**) and adding a ReLU and max pooling layer (**c**) to the neutral network architecture. ReLu and max pooling layer could be realized by adding additional diodes and comparators, respectively, to the hardware architecture.

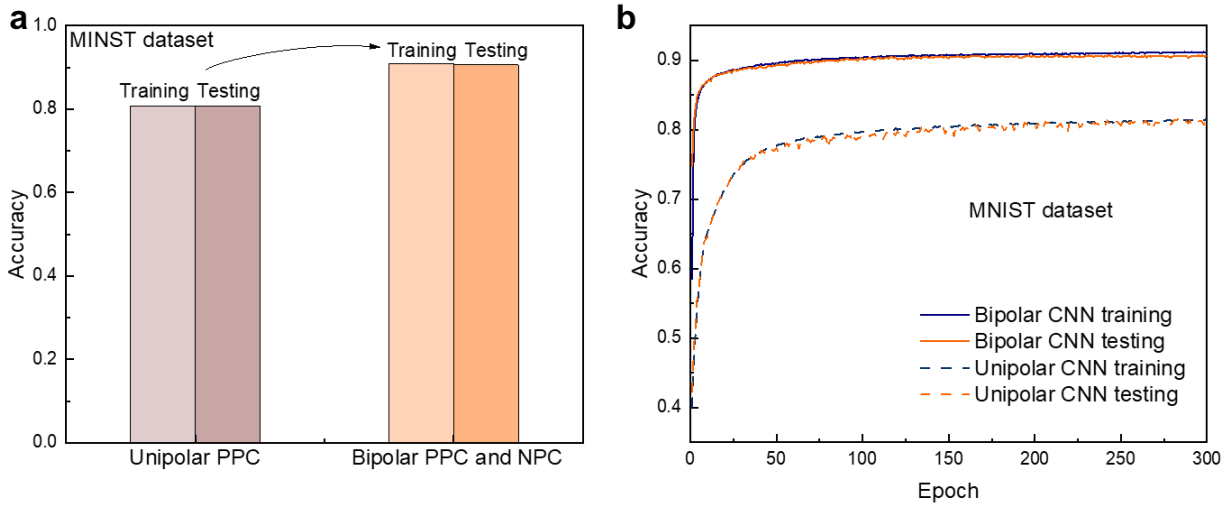

Figure S45. Results of in-sensor classification accuracy based on bipolar photoconductive effect and unipolar photoreconductive effect with standard MNIST dataset.

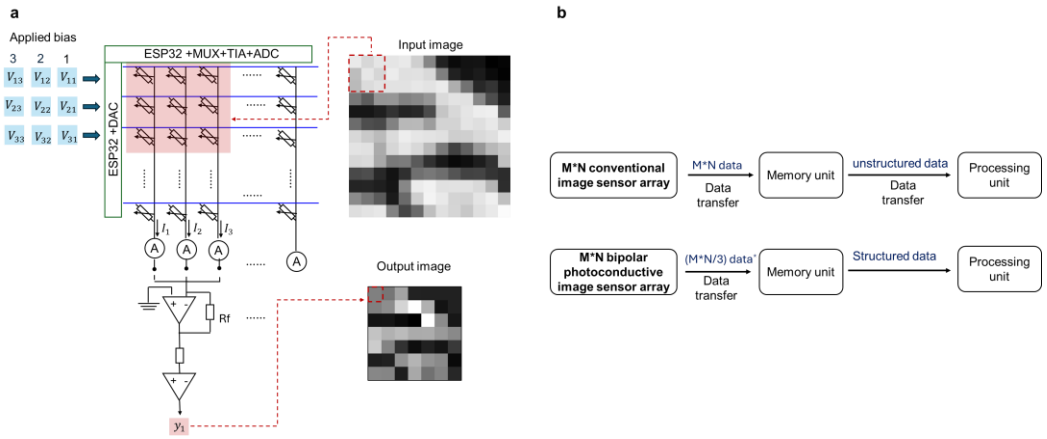

Figure S46. **a**, Schematic illustration of signal acquisition with in-sensor convoluted. **b**, Data flow diagram from sensor node to processing unit. * Assum a 3×3 kernel is applied.

Downloaded from pubs.acs.org/ancac3/article-supplement/5207499/pdf/nn6c07332_si_001/ by PURDUE UNIV user on 28 October 2026

Table S1. Category of bipolar photoconductive devices with trigger mechanisms

Optoelectronic devices with bipolar photoresponse behavior		
Triggering mechanism	**Multidimensional light feature control** • Wavelength[59-61] • Intensity[62] …	**Electrically modulated negative/positive photoresponsivity** • Gate voltage • Pre-polarized voltage …
Promising applications	**All optical controlled logic gate** • All optical computing and all optical network with high speed, wide bandwidth, etc.	**Reconfigurable vision sensor** • Ultrafast machine vision with in-sensor image processing mimic neuro-biological architectures • Retina prosthesis with retinomorphic light encoding

Table S2. Comparison with other reported bipolar photoconductive optoelectronic devices with electrically tunable negative/positive photoresponsivity

Active materials	Mechanism	Trigger methods	Structure[a]	Fabrication technique	Operation condition	Incident light	Responsivity	Array size	Device reproducibility	Stability		Application	Fill factor[b]
										Cycling Stability	Environmental stability		
WSe2 lateral p–n junction[17]	Spit-gate modulated PN or NP	Spilt-gate voltage	4T	ALD, mechanically exfoliated	V_G=-0.25V~+0.25V, V_{DS}=0V	650nm	60 mA/W~~60 mA/W	3×3	27	N/P	N/P	Encoder and classifier	0.18
WSe_2/h-BN/Al_2O_3 hetero structure[26]	Photogating	Gate voltage	3T	Mechanical exfoliation	V_G=0V/-9V, V_{DS}=10mV	405 and 650 nm	N/P	13	5	N/P	N/P	Encoder and classifier	N/P
BP/Al2O3/WSe2/h-BN heterostructure[27]	Photogating	Gate voltage	3T	ALD and mechanical exfoliation	V_G=+5V/-6V, V_{DS}=0.6V	450, 520, and 637 nm	N/P	3×3	9	N/P	9 days	Encoder	0.16
PdSe2/MoTe2 heterostructures[28]	Photogating	Gate voltage	3T	Mechanical exfoliation	V_G = ±10V, V_{DS}=0V	365 nm, 532 nm, 980 nm	100 mA/W~~300mA/W (532nm)	N/P	3	N/P	N/P	Encoder and classifier	N/P
Perovskite-Gated AlGaN/GaN[29]	Photogating	Gate voltage	3T	MOCVD, ALD, spin-coat	V_G=+5V/-6V, V_{DS}=0.1V	457 nm, 532 nm and 660 nm	2*106 A/W (532nm)	N/P	N/P	30	N/P	Encoder	N/P
ReS2/h-BN/MoS2 vdW heterostructure[30]	Photogating	Gate voltage	3T	Mechanical exfoliation	V_G=±30V, V_{DS}=0.1V	520, 637, 830, and 1310 nm	N/P	N/P	N/P	N/P	N/P	N/P	N/P

Downloaded from pubs.acs.org/ancac3/article-supplement/5207499/pdf/nn6c07332_si_001/ by PURDUE UNIV user on 28 October 2026

Graphene/organic heterostructure(PM6:Y6)[31]	Photogating	Gate voltage	3T	Wet transfer, spin coating	V_G=+5V/-20V, V_{Ds}=0.1V	450~1064 nm	2.86 × 106 A W−1	N/P	8	N/P	N/P	Encoder	N/P
WSe2/Al2O3/HfO2/Al2O3[32]	Photogating	Gate voltage	4T	ALD and mechanical exfoliation	V_G=± 6V, V_{DS}=±1V	450 nm, 660 nm	50 mA/W~~60 mA/W	3×3	18	N/P	N/P	Motion recognition	0.19
WSe2–hBN[33]	Photogating	Gate voltage	3T	Mechanical exfoliation, CVD	V_G=±25V, V_{DS}=±1V	532 nm	450mA/W~~450mA/W	N/P	3	N/P	N/P	Encoder	0.18
MoS2/sr-SiNx[34]	Photogating	Gate voltage	3T	Exfoliated, low-pressure CVD	V_G=±3 V, V_{DS}=0.2~0.8V	405, 520, 638 and 940 nm	N/P	18×18	64	50	N/P	Motion recognition	0.013
Epitaxial Pb(Zr0.2Ti0.8)O3[58]	Ferroelectric polarization	Preprogramming	2T	PLD growth	Preprogramming V=-1.94V~+1.89V	365 nm	0.22 mA/W~~0.22mA/W	2×2 and 1×9	11	10^6	N/P	Encoder and classifier	N/P
P(VDF-TrFE)/HfO2[63]	Ferroelectric polarization	Preprogramming	2T	ALD, drop casting	Preprogramming V=+5V/-10V, Operation V=-0.1~~1V	365 nm	N/P	N/P	9	100	N/P	Encoder and classifier	N/P
Se/SWCNT[64]	Photogating	Gate voltage	3T	ALD, immerse deposition	V_G=±8 V, V_{DS}=0.1~1V	375, 405, 532 nm	N/P	10×10	1000	N/P	N/P	In-sensor recognition	0.0089
a-Sb_2O_3/a-Ga_2O_3[65]	Carrier trapping at heterojunction interface	Bias and wavelength	2T	Sputtering	V=0~1V	287 and 303 nm	1.05 mA/W (303nm), -0.71 mA/V (287nm)	N/P	12	40	N/P	Optical communication	N/P
n-PBDF (This work)	**Light-modulated Schottky barrier**	**Bias**	**2T**	**Spin-coating**	**V<±0.2 V**	**405, 532, 650, 808, and 905 nm**	**6.1mA/W~~0.87 mA/W**	20×20 and **62×52**	**87**	**10^6**	**78 days**	**Encoder and classifier**	**0.69 and 0.81**

[a]: 2T: Two terminal, 3T: Three terminal, 4T: Four terminal.
[b]: Extracted from the device image with scale bar.

Table S3. Tradeoff comparison between conventional photodiode and the proposed device in this work

Metric	**Conventional photodiode**	**Proposed device**
Detectivity	High	Relatively low
Structure	PN or PiN junctions	Schottky junction
Operation mode	Photoconductive or photovoltaic	Photoconductive
Materials	Mainly Silicon-based	Conducting polymer (e.g., n-PBDF)
Thickness	Micrometers	Nanometers
Tunable positive/negative photoresponsivity	No	Yes
In-sensor image processing function	No	Yes
Flexibility	Limited	Good
Integration	Conventional sensing system	Neuromorphic sensing system

Downloaded from pubs.acs.org/ancac3/article-supplement/5207499/pdf/nn6c07332_si_001/ by PURDUE UNIV user on 28 October 2026

References

1. Euler, T.;Haverkamp, S.;Schubert, T., Baden, T., Retinal bipolar cells: elementary building blocks of vision. *Nat. Rev. Neurosci.* **2014**, 15, 507-519
2. Tadmor, Y., Tolhurst, D., Calculating the contrasts that retinal ganglion cells and LGN neurones encounter in natural scenes. *Vision research* **2000**, 40, 3145-3157
3. Lagnado, L., Retinal processing: amacrine cells keep it short and sweet. *Current biology* **1998**, 8, R598-R600
4. Gaynes, J. A.;Budoff, S. A.;Grybko, M. J.;Hunt, J. B., Poleg-Polsky, A., Classical center-surround receptive fields facilitate novel object detection in retinal bipolar cells. *Nat. Commun.* **2022**, 13, 5575
5. Zapp, S. J.;Nitsche, S., Gollisch, T., Retinal receptive-field substructure: scaffolding for coding and computation. *Trends Neurosci.* **2022**, 45, 430-445
6. Hubel, D. H., The visual cortex of the brain. *Sci. Am.* **1963**, 209, 54-63
7. Yao, P.;Wu, H.;Gao, B.;Tang, J.;Zhang, Q.;Zhang, W.;Yang, J. J., Qian, H., Fully hardware-implemented memristor convolutional neural network. *Nature* **2020**, 577, 641-646
8. O'shea, K., Nash, R., An introduction to convolutional neural networks. *arXiv preprint arXiv:1511.08458* **2015**,
9. Lindsay, G. W., Convolutional neural networks as a model of the visual system: Past, present, and future. *Journal of cognitive neuroscience* **2021**, 33, 2017-2031
10. Yang, Y.;Wang, Y.;Zhu, C.;Xie, Z.;Qin, Z.;Wang, Z., Chai, Y., Bioinspired and biointegrated vision for artificial sight convergence. *Nature Reviews Bioengineering* **2025**, 1-16
11. Atchison, D., *Optics of the human eye*. (CRC Press, 2023).
12. Takahashi, S.;Huang, Y.-M.;Sze, J.-J.;Wu, T.-T.;Guo, F.-S.;Hsu, W.-C.;Tseng, T.-H.;Liao, K.;Kuo, C.-C., Chen, T.-H., A 45 nm stacked CMOS image sensor process technology for submicron pixel. *Sensors* **2017**, 17, 2816
13. Lahav, A.;Fenigstein, A.;Strum, A., Rizzolo, S., Backside illuminated (BSI) complementary metal-oxide-semiconductor (CMOS) image sensors. *High Performance Silicon Imaging* **2020**, 95-117
14. Wang, S.;Jiang, C.;Yu, Y.;Zhang, Z.;Quhe, R.;Yang, R.;Tian, Y.;Chen, X.;Fan, W., Niu, Y., Tellurium nanowire retinal nanoprosthesis improves vision in models of blindness. *Science* **2025**, 388, eadu2987
15. Ma, Y.;Chen, Y.;Wang, S.;Chen, Z.-H.;Zhang, Y.;Huang, L.;Zhang, X.;Yin, F.;Wang, Y., Yang, M., Near-infrared spatiotemporal color vision in humans enabled by upconversion contact lenses. *Cell* **2025**, 188, 3375-3388. e3318
16. Bourlai, T.;Von Dollen, J.;Mavridis, N., Kolanko, C., in *Infrared imaging systems: design, analysis, modeling, and testing XXIII*. (SPIE, 2012), vol. 8355, pp. 460-471.
17. Mennel, L.;Symonowicz, J.;Wachter, S.;Polyushkin, D. K.;Molina-Mendoza, A. J., Mueller, T., Ultrafast machine vision with 2D material neural network image sensors. *Nature* **2020**, 579, 62-66
18. Pecunia, V.;Anthopoulos, T. D.;Armin, A.;Bouthinon, B.;Caironi, M.;Castellanos-Gomez, A.;Chen, Y.;Cho, K.;Clegg, C., Fang, X., Guidelines for accurate evaluation of photodetectors based on emerging semiconductor technologies. *Nat. Photonics* **2025**, 1-11
19. Jansen-van Vuuren, R. D.;Armin, A.;Pandey, A. K.;Burn, P. L., Meredith, P., Organic photodiodes: the future of full color detection and image sensing. *Adv. Mater.* **2016**, 28, 4766-4802
20. Li, H.;Wang, S.;Zhang, X.;Wang, W.;Yang, R.;Sun, Z.;Feng, W.;Lin, P.;Wang, Z., Sun, L., Memristive crossbar arrays for storage and computing applications. *Advanced Intelligent Systems* **2021**, 3, 2100017
21. Alshaya, A.;Malik, A.;Mifsud, A., Papavassiliou, C., in *Journal of Physics: Conference Series*. (IOP Publishing, 2023), vol. 2613, pp. 012010.
22. Park, S.;Lim, Y.;Heo, C.-J.;Yun, S.;Leem, D.-S.;Kim, S.;Choi, B., Park, K.-B., Transparent organic photodiodes for high-detectivity CMOS image sensors. *Optica* **2022**, 9, 992-999
23. Theuwissen, A., CMOS image sensors. *Smart Sensor Systems: Emerging Technologies and Applications* **2014**, 173-189
24. Xia, Q., Yang, J. J., Memristive crossbar arrays for brain-inspired computing. *Nat. Mater.* **2019**, 18, 309-323
25. Choi, S.;Kang, C.-m.;Byun, C.-W.;Cho, H.;Kwon, B.-H.;Han, J.-H.;Yang, J.-H.;Shin, J.-W.;Hwang, C.-S., Cho, N. S., Thin-film transistor-driven vertically stacked full-color organic light-emitting diodes for high-resolution active-matrix displays. *Nat. Commun.* **2020**, 11, 2732
26. Wang, C.-Y.;Liang, S.-J.;Wang, S.;Wang, P.;Li, Z. a.;Wang, Z.;Gao, A.;Pan, C.;Liu, C., Liu, J., Gate-tunable van der Waals heterostructure for reconfigurable neural network vision sensor. *Sci. Adv.* **2020**, 6, eaba6173
27. Zhang, Z.;Wang, S.;Liu, C.;Xie, R.;Hu, W., Zhou, P., All-in-one two-dimensional retinomorphic hardware device for motion detection and recognition. *Nat. Nanotechnol.* **2022**, 17, 27-32

Downloaded from pubs.acs.org/ancac3/article-supplement/5207499/pdf/nn6c07332_si_001/ by PURDUE UNIV user on 28 October 2026

28. Pi, L.;Wang, P.;Liang, S.-J.;Luo, P.;Wang, H.;Li, D.;Li, Z.;Chen, P.;Zhou, X., Miao, F., Broadband convolutional processing using band-alignment-tunable heterostructures. *Nat. Electron.* **2022**, 5, 248-254
29. Hong, X.;Huang, Y.;Tian, Q.;Zhang, S.;Liu, C.;Wang, L.;Zhang, K.;Sun, J.;Liao, L., Zou, X., Two-dimensional perovskite-gated AlGaN/GaN high-electron-mobility-transistor for neuromorphic vision sensor. *Adv. Sci.* **2022**, 9, 2202019
30. Wang, Y.;Liu, E.;Gao, A.;Cao, T.;Long, M.;Pan, C.;Zhang, L.;Zeng, J.;Wang, C., Hu, W., Negative photoconductance in van der Waals heterostructure-based floating gate phototransistor. *ACS nano* **2018**, 12, 9513-9520
31. Han, C.;Liu, X.;Han, X.;He, M.;Han, J.;Zhang, H.;Hou, X.;Zhou, H.;Yu, H., Wu, Z., High-Performance Phototransistor Based on Graphene/Organic Heterostructure for In-Chip Visual Processing and Pulse Monitoring. *Adv. Funct. Mater.* **2022**, 32, 2209680
32. Zhou, Y.;Fu, J.;Chen, Z.;Zhuge, F.;Wang, Y.;Yan, J.;Ma, S.;Xu, L.;Yuan, H., Chan, M., Computational event-driven vision sensors for in-sensor spiking neural networks. *Nat. Electron.* **2023**, 6, 870-878
33. Han, Z.;Zhang, Y.;Mi, Q.;You, J.;Zhang, N.;Zhong, Z.;Jiang, Z.;Guo, H.;Hu, H., Wang, L., Reconfigurable homojunction phototransistor for near-zero power consumption artificial biomimetic retina function. *ACS nano* **2024**, 18, 29968-29977
34. Pang, X.;Wang, Y.;Zhu, Y.;Zhang, Z.;Xiang, D.;Ge, X.;Wu, H.;Jiang, Y.;Liu, Z., Liu, X., Non-volatile rippled-assisted optoelectronic array for all-day motion detection and recognition. *Nat. Commun.* **2024**, 15, 1613
35. Dodda, A.;Jayachandran, D.;Pannone, A.;Trainor, N.;Stepanoff, S. P.;Steves, M. A.;Radhakrishnan, S. S.;Bachu, S.;Ordonez, C. W., Shallenberger, J. R., Active pixel sensor matrix based on monolayer MoS2 phototransistor array. *Nat. Mater.* **2022**, 21, 1379-1387
36. Cui, B.;Xing, Y.;Han, J.;Lv, W.;Lv, W.;Lei, T.;Zhang, Y.;Ma, H.;Zeng, Z., Zhang, B., Negative photoconductivity in low-dimensional materials. *Chinese Physics B* **2021**, 30, 028507
37. Buscema, M.;Island, J. O.;Groenendijk, D. J.;Blanter, S. I.;Steele, G. A.;van der Zant, H. S., Castellanos-Gomez, A., Photocurrent generation with two-dimensional van der Waals semiconductors. *Chemical Society Reviews* **2015**, 44, 3691-3718
38. Haque, M. A.;Li, J. L.;Abdelhady, A. L.;Saidaminov, M. I.;Baran, D.;Bakr, O. M.;Wei, S. H., Wu, T., Transition from positive to negative photoconductance in doped hybrid perovskite semiconductors. *Advanced Optical Materials* **2019**, 7, 1900865
39. Lui, C.;Frenzel, A.;Pilon, D.;Lee, Y.-H.;Ling, X.;Akselrod, G.;Kong, J., Gedik, N., Trion-induced negative photoconductivity in monolayer MoS 2. *Physical review letters* **2014**, 113, 166801
40. Bose, R.;Adhikari, A.;Burlakov, V. M.;Liu, G.;Haque, M. A.;Priante, D.;Hedhili, M. N.;Wehbe, N.;Zhao, C., Yang, H., Imaging localized energy states in silicon-doped InGaN nanowires using 4D electron microscopy. *ACS Energy Letters* **2018**, 3, 476-481
41. Ke, Z.;Abtahi, A.;Hwang, J.;Chen, K.;Chaudhary, J.;Song, I.;Perera, K.;You, L.;Baustert, K. N., Graham, K. R., Highly conductive and solution-processable n-doped transparent organic conductor. *J. Am. Chem. Soc.* **2023**, 145, 3706-3715
42. Tang, H.;Liang, Y.;Liu, C.;Hu, Z.;Deng, Y.;Guo, H.;Yu, Z.;Song, A.;Zhao, H., Zhao, D., A solution-processed n-type conducting polymer with ultrahigh conductivity. *Nature* **2022**, 611, 271-277
43. Zhan, F.;Wen, G.;Li, R.;Feng, C.;Liu, Y.;Liu, Y.;Zhu, M.;Zheng, Y.;Zhao, Y., La, P., A Comprehensive Review on Oxygen Vacancies Modified Photocatalysts: Synthesis, Characterization, and Applications. *Physical Chemistry Chemical Physics* **2024**,
44. Zhang, C.;Qi, L.;Chen, Q.;Lv, L.;Ning, Y.;Hu, Y.;Hou, Y., Teng, F., Plasma treatment of ITO cathode to fabricate free electron selective layer in inverted polymer solar cells. *Journal of Materials Chemistry C* **2014**, 2, 8715-8722
45. Ng, K. K., Sze, S. M., *Physics of semiconductor devices*. (Wiley-Interscience Hoboken, NJ, 2007).
46. Liu, Y.;Guo, J.;Zhu, E.;Liao, L.;Lee, S.-J.;Ding, M.;Shakir, I.;Gambin, V.;Huang, Y., Duan, X., Approaching the Schottky–Mott limit in van der Waals metal–semiconductor junctions. *Nature* **2018**, 557, 696-700
47. Tang, Z.-X.;Tang, X.-G.;Liu, Q.-X., Jiang, Y.-P., Light–induced transition of charged carrier transport in symmetric metal–semiconductor–metal contacts. *Results in Physics* **2023**, 47, 106384
48. Gong, X.;Tong, M.;Xia, Y.;Cai, W.;Moon, J. S.;Cao, Y.;Yu, G.;Shieh, C.-L.;Nilsson, B., Heeger, A. J., High-detectivity polymer photodetectors with spectral response from 300 nm to 1450 nm. *Science* **2009**, 325, 1665-1667
49. Zhang, Y.;Hellebusch, D. J.;Bronstein, N. D.;Ko, C.;Ogletree, D. F.;Salmeron, M., Alivisatos, A. P., Ultrasensitive photodetectors exploiting electrostatic trapping and percolation transport. *Nat. Commun.* **2016**,

Downloaded from pubs.acs.org/ancac3/article-supplement/5207499/pdf/nn6c07332_si_001/ by PURDUE UNIV user on 28 October 2026

7, 11924
50. Lai, Y.;Li, H.;Kim, D. K.;Diroll, B. T.;Murray, C. B., Kagan, C. R., Low-frequency (1/f) noise in nanocrystal field-effect transistors. *ACS nano* **2014**, 8, 9664-9672
51. Vandamme, L. K., Hooge, F., What Do We Certainly Know About 1/f Noise in MOSTs? *IEEE Transactions on Electron Devices* **2008**, 55, 3070-3085
52. Ji, P.;Yang, S.;Wang, Y.;Li, K.;Wang, Y.;Suo, H.;Woldu, Y. T.;Wang, X.;Wang, F., Zhang, L., High-performance photodetector based on an interface engineering-assisted graphene/silicon Schottky junction. *Microsystems & Nanoengineering* **2022**, 8, 9
53. Xu, J.;Liu, T.;Hu, H.;Zhai, Y.;Chen, K.;Chen, N.;Li, C., Zhang, X., Design and optimization of tunneling photodetectors based on graphene/Al2O3/silicon heterostructures. *Nanophotonics* **2020**, 9, 3841-3848
54. Sharma, V.;Diba, A.;Neven, D.;Brown, M. S.;Van Gool, L., Stiefelhagen, R., in *Proceedings of the IEEE Conference on Computer Vision and Pattern Recognition*. (2018), pp. 4033-4041.
55. Hanson, S.;Foo, Z.;Blaauw, D., Sylvester, D., A 0.5 V sub-microwatt CMOS image sensor with pulse-width modulation read-out. *IEEE Journal of Solid-State Circuits* **2010**, 45, 759-767
56. Hanson, S.;Zhai, B.;Bernstein, K.;Blaauw, D.;Bryant, A.;Chang, L.;Das, K. K.;Haensch, W.;Nowak, E. J., Sylvester, D. M., Ultralow-voltage, minimum-energy CMOS. *IBM journal of research and development* **2006**, 50, 469-490
57. Wu, W., High-performance CMOS image sensor power supply in industrial camera and vision. *Appl. Rep. Texas Instrum.* **2019**, 1-28
58. Cui, B.;Fan, Z.;Li, W.;Chen, Y.;Dong, S.;Tan, Z.;Cheng, S.;Tian, B.;Tao, R., Tian, G., Ferroelectric photosensor network: an advanced hardware solution to real-time machine vision. *Nat. Commun.* **2022**, 13, 1707
59. Yang, C. M.;Chen, T. C.;Verma, D.;Li, L. J.;Liu, B.;Chang, W. H., Lai, C. S., Bidirectional all-optical synapses based on a 2D Bi2O2Se/graphene hybrid structure for multifunctional optoelectronics. *Adv. Funct. Mater.* **2020**, 30, 2001598
60. Yang, R.;Wang, Y.;Li, S.;Hu, D.;Chen, Q.;Zhuge, F.;Ye, Z.;Pi, X., Lu, J., All-optically controlled artificial synapse based on full oxides for low-power visible neural network computing. *Adv. Funct. Mater.* **2024**, 34, 2312444
61. Jiang, J.;Shan, X.;Xu, J.;Sun, Y.;Xiang, T., Li, A., S. i. Sasaki, H. Tamiaki, Z. Wang, XF Wang. *Adv. Funct. Mater* **2024**, 34, 2409677
62. Cai, B.;Huang, Y.;Tang, L.;Wang, T.;Wang, C.;Sun, Q.;Zhang, D. W., Chen, L., All-Optically Controlled Retinomorphic Memristor for Image Processing and Stabilization. *Adv. Funct. Mater.* **2023**, 33, 2306272
63. Dai, Q.;Pei, M.;Guo, J.;Wang, Q.;Hao, Z.;Wang, H.;Li, Y.;Li, L.;Lu, K., Yan, Y., Integration of image preprocessing and recognition functions in an optoelectronic coupling organic ferroelectric retinomorphic neuristor. *Mater. Horiz.* **2023**, 10, 3061-3071
64. Yao, J.;Wang, Q.;Geng, L.;Zhao, Z.;Zhao, Y.;Teng, Y.;He, Y.;Zhang, Y.;Li, Q., Qiu, S., Gate-Tunable Highly Linear Bipolar Photoresponse in Se@ SWCNT Adaptive Neurons for Dynamically Programmable Neuromorphic Computing. *Adv. Mater.* **2025**, 37, e06367
65. Wu, C.;Lv, P.;Zhu, Z.;Huang, Y.;Tu, C.;Chen, C.;Lakshminarayana, G., Wang, Y., A bipolar response deep ultraviolet photodetector for encryption and anti-interference communication based on an a-Sb 2 O 5/a-Ga 2 O 3 heterojunction. *Mater. Horiz.* **2026**.

Downloaded from pubs.acs.org/ancac3/article-supplement/5207499/pdf/nn6c07332_si_001/ by PURDUE UNIV user on 28 October 2026